J. Fluid Mech. (2012), *vol.* 706, *pp.* 496–533.
doi:10.1017/jfm.2012.273

The fluid dynamics of rolling wheels at low Reynolds number

Sergio Pirozzoli†, Paolo Orlandi and Matteo Bernardini

Dipartimento di Ingegneria Meccanica e Aerospaziale, Università di Roma 'La Sapienza', via Eudossiana 18, 00184 Roma, Italy

(Received 23 December 2011; revised 2 May 2012; accepted 5 June 2012; first published online 20 July 2012)

We study the fluid dynamics of rolling wheels at Reynolds number $Re_D \leqslant 1000$ (where Re_D is the Reynolds number based on the wheel diameter), with the objective of characterizing the various regimes of steady and unsteady motion. Regardless of the Reynolds number, the flow is found to separate approximately 10° upstream of the apex of the wheel, where a saddle point in the pseudo-streamtrace pattern is observed. Under the flow conditions here essayed, the drag coefficient steadily decreases with Re_D, and the lift coefficient remains strictly positive. The positive lift provided by the rolling wheel is associated with the presence of a strong (positive) peak of the static pressure in the upstream proximity of the contact point with the ground, which we interpret as the result of the impingement of flow particles entrained in the boundary layer that develops on the front part of the wheel. Steady laminar flow is observed up to $Re_D \approx 300$, which is characterized by a three-dimensional wake whose length increases with the Reynolds number. Unsteadiness is first observed at $Re_D \approx 400$, under which conditions the flow retains planar symmetry, and is characterized by the quasi-periodic shedding of hairpin vortices. Transition to three-dimensional flow happens at $Re_D \approx 500$, in which case a sinuous mode of instability in the wheel wake is established, which modulates the shedding of the hairpins, and which causes the onset of a non-zero side force. At the highest Reynolds number considered here ($Re_D = 1000$) the wake exhibits some characters of turbulence, with wide-band frequency spectra, and its topology entirely changes, becoming split into two parts, and being much shortened compared to the lower-Re_D cases. Despite the limitation of the study to low Reynolds numbers we find that, once significant three-dimensionality and scale separation are established in the wheel wake, the nature of the flow becomes qualitatively similar to fully developed turbulent flow. In perspective, this observation opens interesting avenues for the prediction of unsteady flow around rotating tyres at moderate computational cost.

Key words: computational methods, separated flows, vortex shedding

1. Introduction

The flow around objects of complex shape, and in the presence of solid boundaries, is a subject of the utmost interest in aerodynamic applications. Most of our knowledge of massively separated flows behind blunt-shaped objects derives from basic studies performed on prototype geometries, such as cylinders and spheres. The aerodynamics

† Email address for correspondence: sergio.pirozzoli@uniroma1.it

of cylinders in particular has attracted the attention of scientists, and it has been the subject of dedicated reviews (Williamson 1996) because of the extremely rich variety of the flow structures. The flow around a cylinder in an unbounded incompressible fluid is parametrized by the Reynolds number (for instance based on the cylinder diameter, Re_D), and it is well known that different flow patterns may occur as Re_D is varied. Steady laminar flow exists at Reynolds numbers up to $Re_D \approx 40$, with a pair of symmetric counter-rotating vortices forming behind the cylinder at $Re_D > 5$. Nominally two-dimensional vortex shedding is observed up to $Re_D \approx 190$, beyond which fully three-dimensional flow is observed. The shear layers separating from the cylinder become unstable at $Re_D \approx 1200$, and for $Re_D \geqslant 3.5 \times 10^6$ the boundary layer on the surface of the cylinder becomes turbulent before separation, yielding a lower base suction coefficient and lower drag due to delayed separation.

Although interesting from an academic standpoint, the flow around a spanwise infinite cylinder is of limited practical interest, since any real object has finite aspect ratio. In this respect, the flow around a sphere is the simplest prototype of flow around a compact body. Although not as widely studied as the cylinder flow, the sphere has been the subject of several numerical and experimental studies, which have highlighted dynamics other than the cylinder, and several regimes have been identified which depend sensitively on the Reynolds number. The presence of solid walls adds a degree of complexity to the problem, qualitatively changing the flow behaviour, as highlighted in several recent studies (Stewart *et al.* 2010*a*,*b*; Rao *et al.* 2012).

Although of extreme interest for industrial applications (the most obvious being car tyre aerodynamics), the flow around a finite cylinder (hereafter referred to as a wheel) in contact with the ground has never been previously investigated from a fundamental point of view. Part of the reason may reside in its intrinsic geometric complexity, which limits the application of body-fitted numerical methods, and in the difficulty in correctly reproducing the perfect rolling condition both numerically and experimentally. All previous related studies were focused on real tyre geometries (with inherent complications for computational fluid dynamics, CFD), and Reynolds numbers in the range $Re_D = 10^5$–10^6, which is of interest for automotive engineering. The evidence of experimental studies is quite contradictory, and apparently there is no consensus on very fundamental issues, such as the geometric properties of the wake (not even in the time-average sense) and on the direction of the vertical force, some authors claiming that a down-force should be present, and others (the majority) supporting the occurrence of positive lift. Early studies (Cogotti 1983) pointed to the sensitivity of the flow, in particular the sensitivity of the lift coefficient, to the details of the experimental arrangement, and especially to the presence of a small gap between the tyre and the wall, which may yield negative values for the lift coefficient (Morelli 1969). Cogotti (1983) speculated that the wake vortex system consists of three pairs of counter-rotating vortices, two shed from the upper edge of the wheel, two from the tyre hub (if present), and two weaker ones caused by the splatting of fluid at the front surface of the wheel. Through a particle image velocimetry (PIV) study, Saddington, Knowles & Knowles (2007) found that only two counter-rotating vortex pairs are present in the tyre wake, which both induce motion towards the wall in between, and sufficiently far from the tyre only the near-wall pair survives. These facets of the fluid dynamics of wheels have important practical implications for the aerodynamic design of cars, especially those made to operate with exposed tyres, as is the case for racing cars (Katz 2006), for which the drag force associated with rolling tyres may amount to up to 40 % of the total drag.

Computational studies of rolling wheels are very rare in the open literature, and to our knowledge, the only relevant studies are those of McManus & Zhang (2006) and Axerio *et al.* (2009). The former study is based on Reynolds-averaged Navier–Stokes (RANS) modelling of turbulence, which only yields information on the mean structure of the flow field. Those authors discussed the topology of the flow around a realistic tyre, highlighting the differences between the cases of stationary and rolling wheels, and observing that in the latter case only two counter-rotating vortices appear in the tyre wake. The only instance of unsteady simulation of flow around a tyre was reported by Axerio *et al.* (2009), who performed a large-eddy simulation (LES) at realistic operating conditions, unfortunately only for the case of stationary tyres, which is fundamentally different from that of rolling tyres.

In this paper we aim to study the aerodynamics of wheels rolling (without slipping) on a solid wall through numerical simulations. For that purpose we intentionally avoid the use of any turbulence model, and perform direct numerical simulation (DNS) of the governing flow equations. As a consequence, the study is limited to low Reynolds numbers ($Re_D \leqslant 1000$), which are far from realistic operating conditions. The study is carried out with a compressible flow solver, which also allows us to establish the influence of Mach number variation (albeit weak in the range of flow conditions of interest for the car industry). The paper is organized as follows. In § 2 we present the numerical method used for the analysis, which is then validated through comparison with other studies in § 3. The results obtained for flow around a rolling wheel are presented in § 4, and concluding remarks are given in § 5.

2. Numerical method

The flow solver used for the numerical study was previously applied to the analysis of compressible wall-bounded turbulence in the presence of shock waves (Pirozzoli 2011; Pirozzoli & Bernardini 2011). The key ingredient of the code is a dissipation-free finite-difference discretization of the convective terms in the Navier–Stokes equations capable of guaranteeing exact discrete kinetic energy preservation in the limit of inviscid incompressible flow, which makes the discretization compatible with the analytical secondary conservation properties. We stress that this is a mandatory prerequisite for the accurate prediction of turbulent and transitional flows. The inclusion of the compressibility effects (although weak) allows the extraction of additional information related to the acoustic radiation of the flow, which will be the subject of a separate study. The main limitation of using a compressible solver to study flow cases where the Mach number is typically very low ($M_\infty \leqslant 0.3$) is some degree of inefficiency, given the time step restriction associated with the necessity to resolve the time evolution of acoustic waves, which become much faster than hydrodynamic waves when the Mach number is much less than unity. However, the use of a compressible flow solver avoids the solution of the Poisson equation for pressure, which greatly facilitates implementation on massively parallel computers and the use of mesh stretching in all coordinate directions. To alleviate the computational effort involved in numerical simulations, the study of the rolling wheel is carried out at $M_\infty = 0.3$. Although this is at the higher end of the Mach number range of interest for racing cars, the compressibility effects are still very weak (as later shown for the simulations of flow around a sphere), and we expect that the results are representative of the whole low-Mach-number range.

The main addition to the baseline flow solver is the inclusion of an immersed boundary capability, i.e. the ability to deal with embedded geometries with arbitrary

shape on a Cartesian grid. The immersed boundary (IB) method is here implemented following the approach proposed by Fadlun *et al.* (2000), and modified by de Palma *et al.* (2006) for steady compressible flows. Specifically, at each Runge–Kutta substep the velocity at grid points lying inside the body is modified to make it consistent with the local body velocity, which is zero in the case of a stationary body, and equal to the local rotation velocity for the case of a rolling wheel. Furthermore, the velocity at the fluid points nearest to the body surface is extrapolated in such a way that the no-slip condition is satisfied at the boundary points, thus providing second-order accuracy in the boundary treatment. The solver is capable of reading CAD geometry files in the stereolithography (STL) format. Then, a preprocessor based on a ray-tracing algorithm (O'Rourke 1998) discriminates between inner and outer points. One of the many advantages of the IB method consists in the fact that the estimation of the global aerodynamic forces acting on immersed bodies is straightforward. Here we follow the approach proposed by Taira & Colonius (2007), and determine lift, drag and side forces by summing the equivalent body forces at the interior and boundary nodes of the immersed objects.

Regarding the numerical boundary conditions, locally one-dimensional characteristic decomposition is used at the boundary points to discriminate between incoming and outgoing waves. At the inlet and far-field boundaries the amplitude of the incoming waves is then estimated assuming relaxation to the free-stream conditions (Poinsot & Lele 1992). As also proposed by Poinsot & Lele (1992), the effect of the bottom wall is accounted for by enforcing perfect reflection of the impinging acoustic waves. More details on the computational arrangement used for the study of the flow around a rolling wheel are given in § 4.

3. Code validation tests

3.1. *Flow around a rotating cylinder*

As a preliminary step, we consider the two-dimensional flow around a rotating cylinder, which is widely documented in the literature. In the incompressible case the flow is parametrized through the Reynolds number $Re_D = u_\infty D/\nu_\infty$, and the non-dimensional rotation rate $\alpha = \Omega R/u_\infty$, where R and D are the cylinder radius and diameter, respectively, and Ω is the imposed cylinder rotation rate (assumed positive when anticlockwise). In the compressible case that we are dealing with a further independent parameter is the free-stream Mach number $M_\infty = u_\infty/c_\infty$. The mesh used for the simulations covers the rectangular domain $[-15R : 25R] \times [-20R : 20R]$, and it has a resolution of $\sim$30 points per radius near the cylinder.

The early stages in the flow evolution (at $\alpha = 0.5$, $Re_D = 1000$) starting from rest are addressed in figure 1, where the computed instantaneous streamlines are reported at various non-dimensional times, $\tau = tu_\infty/D$. At early times ($\tau = 3$) two eddies form behind the cylinder because of boundary layer separation, which induce secondary, counter-rotating eddies near the cylinder, clearly visible at $\tau = 4$. The main effect of the imposed rotation is a clear asymmetry in the flow pattern, apparent in the faster growth of the upper eddy, which is eventually shed off the cylinder at $\tau = 11$. Agreement between the present results (here shown for $M_\infty = 0.3$) and previous computations and experiments (also reported in figure 1) is good. The evolution of the flow over long times eventually leads to a quasi-periodic state, which is addressed next, for $\alpha = 1$, corresponding to a case where the cylinder's peripheral velocity equals the free-stream velocity. The computed instantaneous flow patterns at $Re_D = 100, 200$ are shown in figure 2, where vorticity contours are plotted. As has also been found

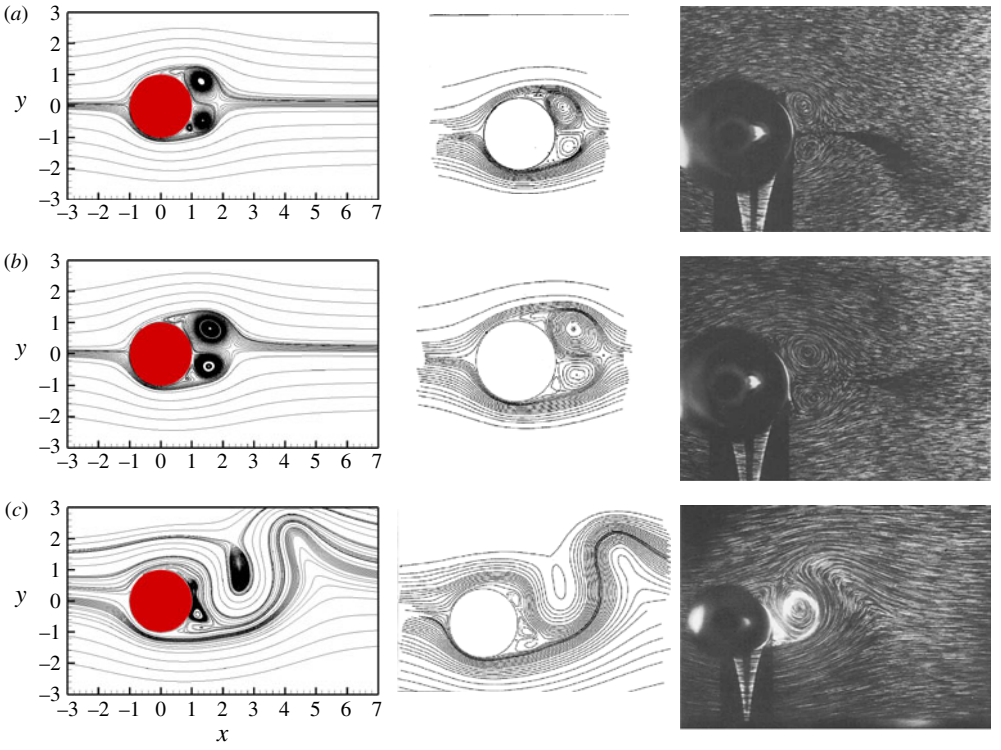

FIGURE 1. (Colour online) Flow around an impulsively started rotating cylinder at $Re_D = 1000$, $\alpha = 0.5$, $M_\infty = 0.3$: (*a*) $\tau = 3$, (*b*) $\tau = 4$, (*c*) $\tau = 11$. Comparison between present data (left column), numerical simulations by Mittal & Kumar (2003) (middle column), and experiments by Badr *et al.* (1990) (right column).

by previous investigators, the flow is similar to that around a steady cylinder, with quasi-periodic shedding of eddies of opposite sign on either side of it. One should note, however, that eddies tend to be shed in the positive half-plane, consistent with the direction of the cylinder rotation. Further, it can be seen that the spacing of the eddies is decreased as Re_D increases, reflecting the increase of the shedding frequency. The numerical results are compared with incompressible simulations by Kang *et al.* (1999) and Mittal & Kumar (2003) in figure 3, where we show the mean lift and drag coefficients, $c_l = F_y/(\rho_\infty u_\infty^2 R)$, $c_d = F_x/(\rho_\infty u_\infty^2 R)$, and the peak Strouhal number ($St_D = fD/u_\infty$) of the lift coefficient spectrum, all estimated after the flow has reached a statistically steady state. As previously noticed, the Strouhal number has a tendency to increase with Re_D, and the asymmetry of the flow is reflected in a net lift pointing in the negative-y direction. Clearly, the simulations performed at the lower Mach number ($M_\infty = 0.1$) match very well both the incompressible force coefficients and the shedding frequency. On the other hand, the single simulation performed at $M_\infty = 0.3$ yields larger drag, and it somewhat overpredicts the peak Strouhal number. This behaviour is probably due to the effect of finite flow compressibility, which may yield non-negligible variation of the aerodynamic forces even at low free-stream Mach number, especially in the case considered here of two-dimensional flows, in which strong accelerations and decelerations take place. To give an idea, in the case of the

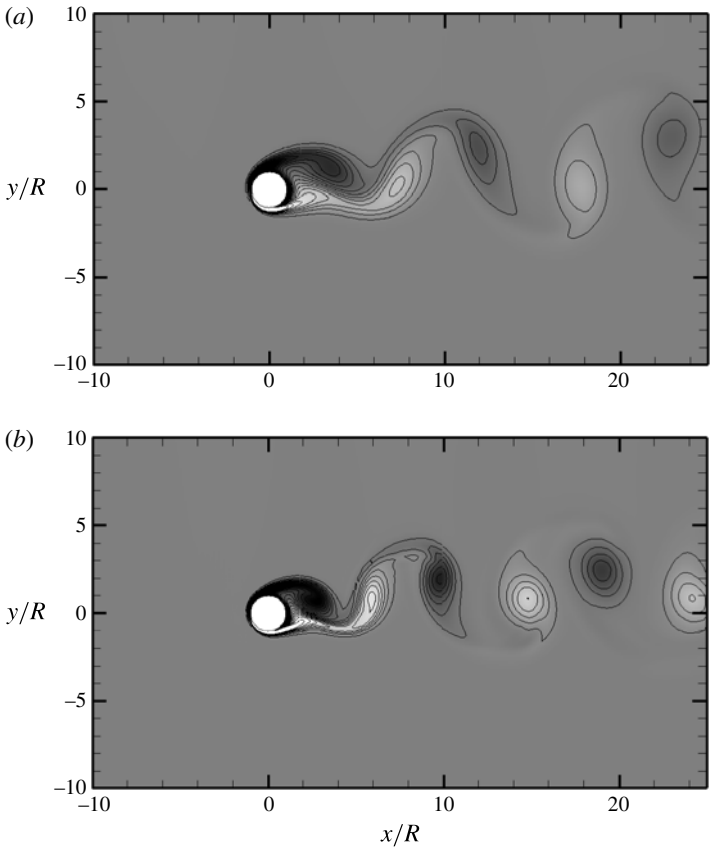

FIGURE 2. Vorticity contours for the flow around a rotating cylinder for $\alpha = 1$ at (*a*) $Re_D = 100$, (*b*) $Re_D = 200$ (in both cases $M_\infty = 0.1$). Sixteen colour levels are shown, with $-4.2 \leqslant \omega D/u_\infty \leqslant 4.2$, the colour scale ranging from black to white.

rotating cylinder simulation at $M_\infty = 0.3$, the maximum Mach number reached within the flow is ∼0.6.

3.2. *Flow around a rolling cylinder*

The flow around a rolling cylinder is a two-dimensional prototype of the flow that we are interested in, and it has been recently investigated (in the incompressible limit) by Stewart *et al.* (2010*b*). Those authors considered rotating cylinders in the very close proximity of a solid wall, which was made to translate with the free-stream velocity. Several cylinder rotation rates were considered, and the influence of the gap height (G) was studied. Regarding the latter issue, those authors were unable to simulate the flow in the case of cylinder in direct contact with the ground ($G = 0$), and noticed weakly singular behaviour of the force coefficients as the gap becomes vanishingly small. Here we directly consider the case of cylinder in contact with the wall, and assume zero slip velocity, which is achieved for $\alpha = 1$. The mesh used for the simulations covers the rectangular domain $[-15R : 30R] \times [-R : 20R]$, and it has a resolution of ∼40 points per radius near the cylinder. The adequacy of the computational mesh was assessed through a grid convergence study of the force coefficients. All simulations

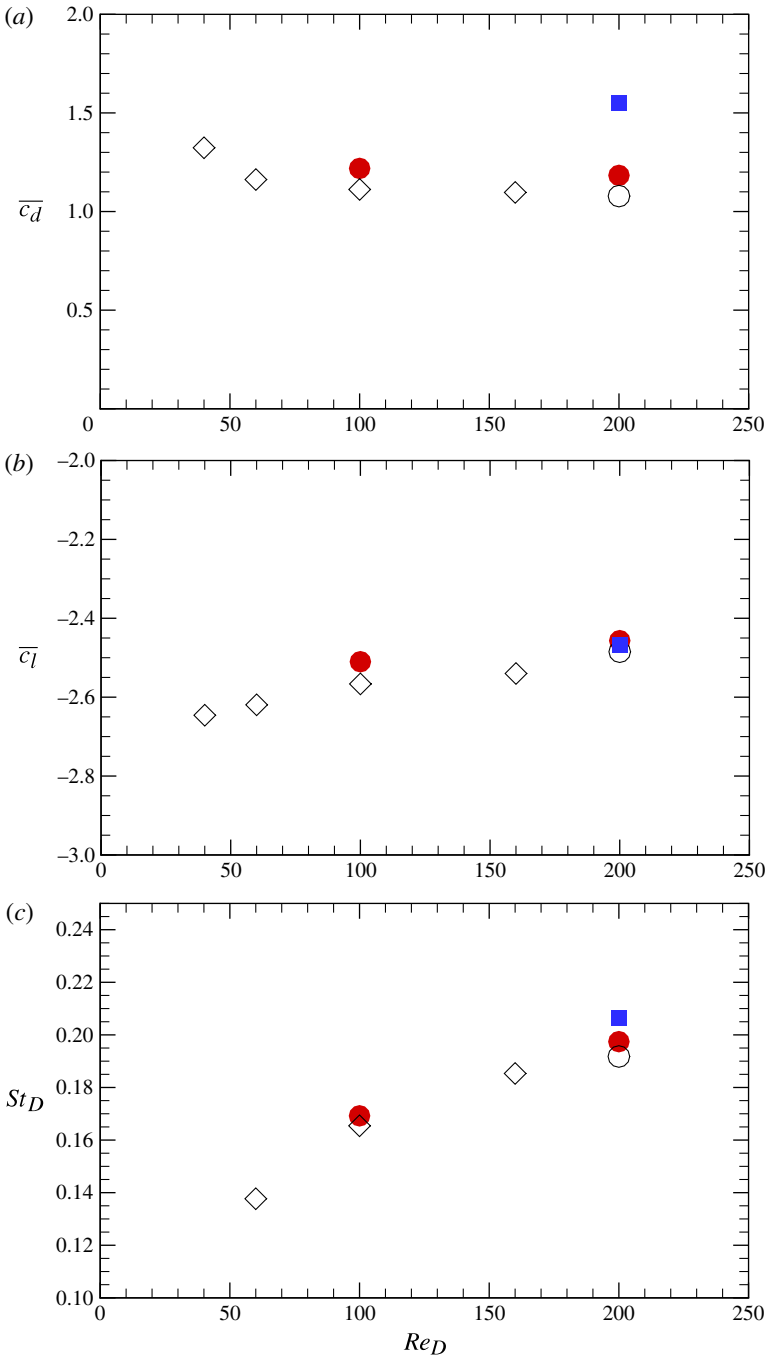

FIGURE 3. (Colour online) (*a*) Drag coefficient, (*b*) lift coefficient and (*c*) Strouhal number for flow around a rotating cylinder at $\alpha = 1$. Solid symbols denote simulations at $M_\infty = 0.1$ (circles), $M_\infty = 0.3$ (squares). Open symbols denote data from other authors: ◇, Kang, Choi & Lee (1999); ○, Mittal (1999*b*).

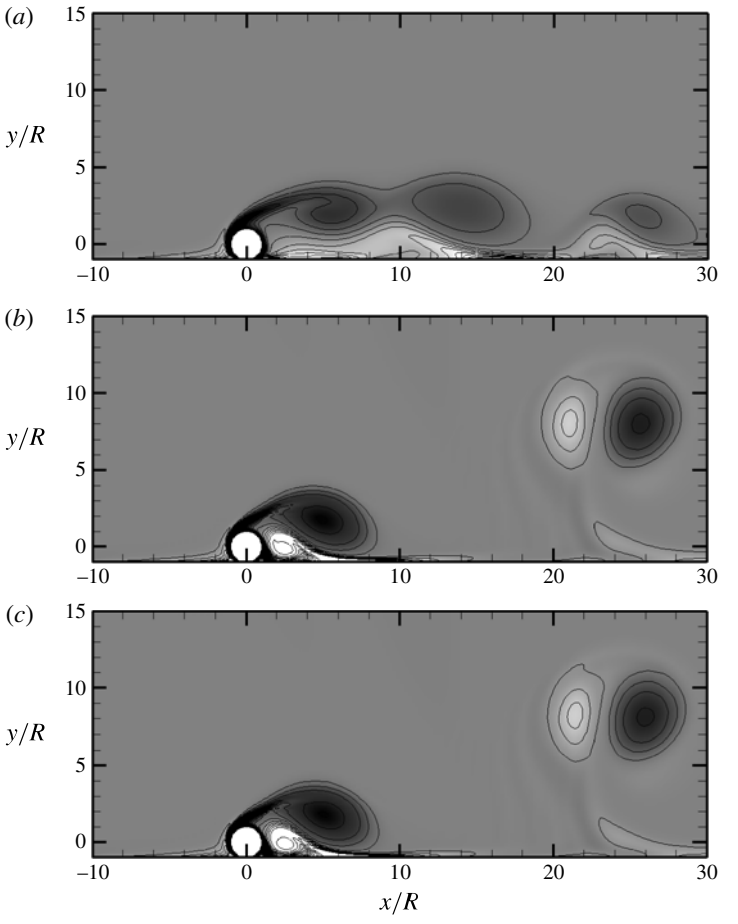

FIGURE 4. Vorticity contours for the flow around a rolling cylinder at (*a*) $Re_D = 100$, (*b*) $Re_D = 200$ (in both cases $M_\infty = 0.1$). Frame (*c*) is the same as (*b*), but in the presence of a small gap ($G/D = 0.005$). Sixteen colour levels are shown, with $-6.8 \leqslant \omega D/u_\infty \leqslant 6.8$, the colour scale ranging from black to white.

are started impulsively, e.g. the velocity is set to its free-stream value throughout, and results are only shown after the flow has reached a statistically stationary state.

The qualitative properties of the flow field can be understood from inspection of figure 4, where instantaneous vorticity contours are shown for $Re_D = 100, 200$ (figure 4*a,b*). As noticed in previous simulations and experiments (Stewart *et al.* 2010*b*), the main effect of the bottom wall is to inhibit the shedding of eddies from the lower side of the cylinder. Clockwise vortices are observed to be shed from the upper edge of the cylinder, which promote the formation of anticlockwise vorticity near the wall because of the no-slip condition (Orlandi 1990). In the case of higher Re_D, the secondary vorticity is observed to couple with the primary one to form vortex dipoles which propel themselves away from the wall. This scenario is entirely consistent with the findings of Stewart *et al.* (2010*b*). To establish the effect of the presence of a finite gap on the computed flow pattern, in figure 4(*c*) we show the results obtained by enforcing a small gap ($G/D = 0.005$, as also considered by those

authors). It can be noted that, by matching the time instant for the comparison, the vorticity field looks virtually indistinguishable from the zero-gap case (compare with figure 4*b*). In figure 5 we show the mean force coefficients and the peak Strouhal numbers determined from the lift coefficient time history. In this case, qualitative agreement with the reference incompressible data is observed for the drag coefficient and for the characteristic flow frequency, but with deviations of ∼20–30 %. Much more critically, the lift coefficient seems to be inaccurate for the incompressible data, especially as M_∞ is lowered. We have then tried to verify whether the observed poor agreement is due to the presence of a finite gap in the data of Stewart *et al.* (2010*b*), and performed additional simulations with $G/D = 0.005$, whose grid-converged results (obtained with 80 points per radius, and 12 points inside the gap zone) are shown in figure 5 with triangle symbols. Although the disparity in the computed c_l is substantially less than in the no-gap case, wide differences persist, which apparently cannot be traced back to lack of resolution of the present data. It is also noteworthy that the $M_\infty = 0.3$ simulation yields reduced drag compared to the $M_\infty = 0.1$ case. After examination of flow snapshots and of the mean fields (not shown here), we have found that this is due to a qualitative modification of the shedding pattern past the cylinder, which translates into a longer recirculation bubble. This is a further demonstration that compressibility effects may play a (often non-trivial) role in the case of two-dimensional flows. As shown in the following, this is not the case for three-dimensional flows.

3.3. *Flow around a sphere*

To test the capabilities of the flow solver to accurately predict three-dimensional flows, we consider the flow around a sphere at $Re_D \leqslant 500$. Despite its apparent simplicity, this flow is extremely rich in terms of flow dynamics, and it constitutes a severe challenge for numerical algorithms. Four flow regimes were identified in previous studies in the Reynolds number range here explored (Johnson & Patel 1999; Mittal 1999*a*; Tomboulides & Orszag 2000). For $Re_D \lesssim 210$, steady axisymmetric flow is recovered, with a recirculation bubble whose length increases with Re_D. At $Re_D \approx 210$ a regular bifurcation occurs, which leads to steady non-axisymmetric flow, characterized by a typical double-thread wake. At $Re_D \approx 270$ a second bifurcation occurs, which leads to an unsteady pattern characterized by regular shedding of hairpin vortices in the sphere wake, symmetric about a plane whose orientation (which depends sensitively on the initial conditions) remains fixed with time. At higher Re_D (transition is reported by Mittal 1999*b* to occur around $Re_D \approx 350$–375) planar symmetry is lost, and the orientation of the hairpins being shed varies randomly in time.

We then performed a set of simulations at representative Reynolds numbers ($Re_D = 100, 250, 300, 350, 500$), and compared the results with data available in the literature. For all the simulations the computational mesh has been selected to be sufficiently wide to minimize the effect of numerical blockage, often quoted as the reason for the scatter in the results of previous authors, the domain extending for $[-15R : 35R] \times [-15R : 15R] \times [-15R : 15R]$ in the three coordinate directions. The mesh is stretched in such a way that the spacing in all coordinate directions is nearly the same around the body, with a resolution of 30 points per sphere radius. The total number of grid points used for the simulations is $512 \times 240 \times 240$, which is found to be sufficient to obtain accurate results at the Reynolds numbers considered here. To compare with results in the literature, all of which deal with incompressible flow, we have performed simulations in the low-Mach-number range, for $M_\infty = 0.1, 0.2, 0.3$.

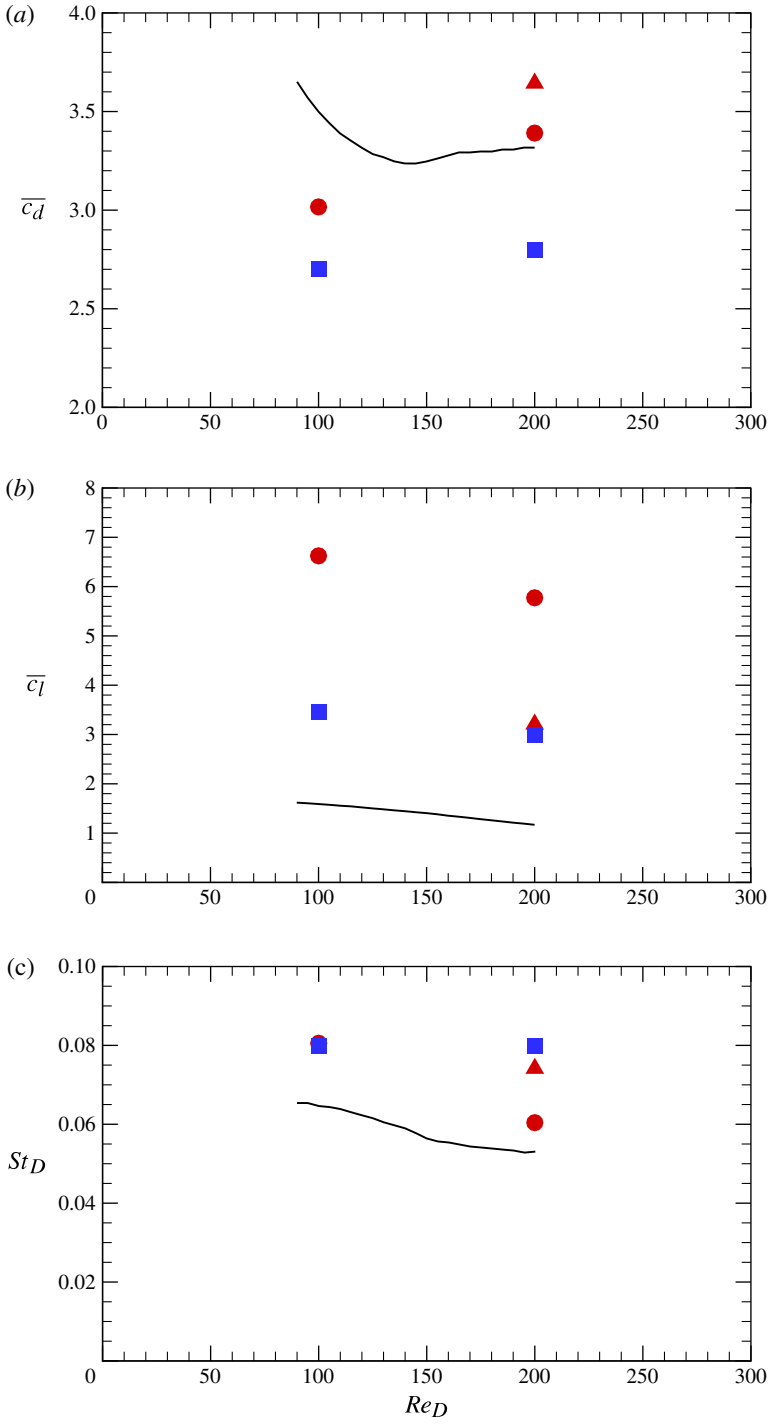

FIGURE 5. (Colour online) (*a*) Drag coefficient, (*b*) lift coefficient and (*c*) Strouhal number for flow around a rolling cylinder. Solid symbols denote our simulations at $M_\infty = 0.1$ (circles), $M_\infty = 0.3$ (squares). The triangles denote the results obtained with a finite gap ($G/D = 0.005$) at $M_\infty = 0.1$. Lines denote data from Stewart *et al.* (2010*b*).

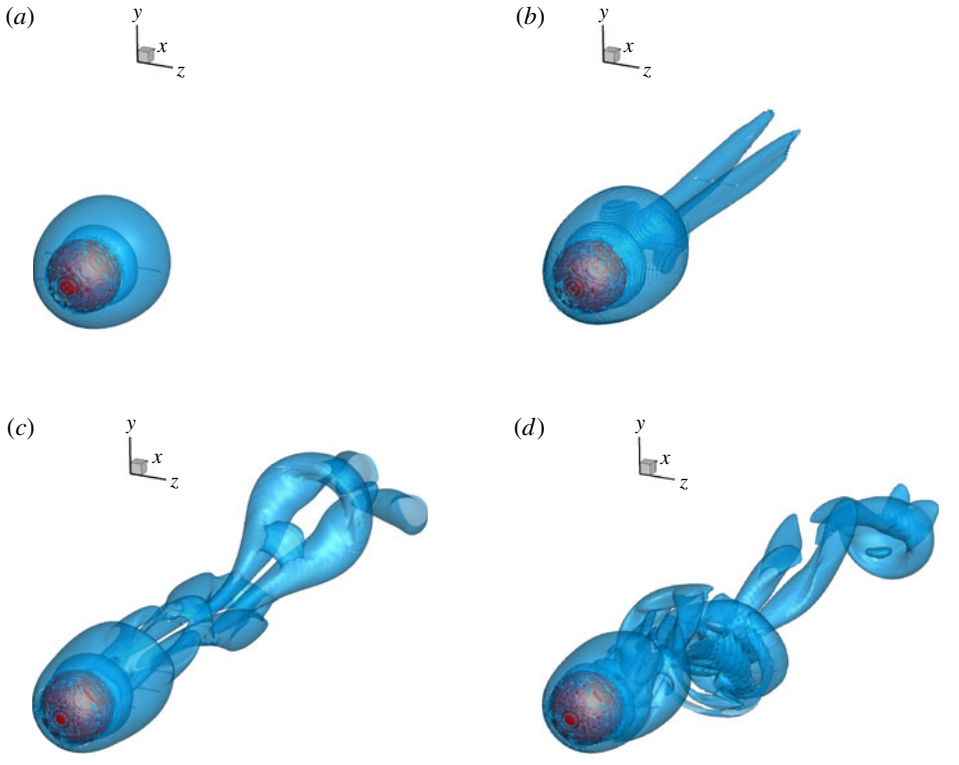

FIGURE 6. (Colour online) Vortical structures (educed through swirling strength iso-surfaces) in the near wake of a sphere at (*a*) $Re_D = 100$ ($\lambda_{c,i} = 0.02u_\infty/D$), (*b*) $Re_D = 250$ ($\lambda_{c,i} = 0.02u_\infty/D$), (*c*) $Re_D = 350$ ($\lambda_{c,i} = 0.42u_\infty/D$), (*d*) $Re_D = 500$ ($\lambda_{c,i} = 0.42u_\infty/D$). for all cases, $M_\infty = 0.1$.

Flow visualizations of representative simulations are shown in figure 6, through iso-surfaces of the swirling strength ($\lambda_{c,i}$), which is the imaginary part of the complex conjugate eigenvalue pair of the velocity gradient tensor, and which allows us to effectively educe flow zones dominated by swirl (Zhou *et al.* 1999). As expected, the simulations performed at $Re_D = 100$ yield stationary, axisymmetric solutions, even though the simulations are started impulsively with free-stream conditions, and random perturbations are initially added to break any possible symmetry. In that case a closed recirculation bubble forms, and no vortex is observed to detach from the sphere surface (figure 6*a*). At $Re_D = 250$ the double-thread wake pattern is observed (figure 6*b*), whose symmetry plane does not rotate significantly during the course of the simulations. Hairpin-shaped vortices are found to be shed at the two higher Reynolds numbers, which retain planar symmetry at $Re_D = 350$ (figure 6*c*), and have more erratic orientation at $Re_D = 500$ (figure 6*d*).

Accurate estimates of the drag coefficient and of the wake length for axisymmetric flow around a sphere were reported by Fornberg (1988), which are compared with the present simulations in table 1. At the lower Mach number the drag coefficient is predicted to within 0.3 % accuracy, as is also the wake length. Weak effects of flow compressibility are observed at higher M_∞. This favourable comparison supports the predictive capability of the numerical algorithm for complex three-dimensional flows.

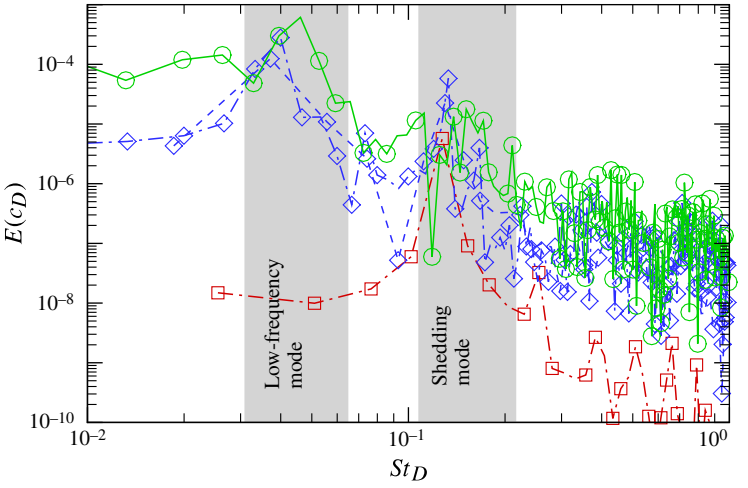

FIGURE 7. (Colour online) Spectra of drag coefficient for flow around a sphere at $Re_D = 300$ (squares), $Re_D = 350$ (diamonds), $Re_D = 500$ (circles), $M_\infty = 0.1$ (solid line), $M_\infty = 0.2$ (dashed line), $M_\infty = 0.3$ (dot-dashed line).

	M_∞	$\bar{c}_D$	L_w/R
Fornberg (1988)	Inc.	1.084	2.744
Present	0.1	1.082	2.688
Present	0.2	1.093	2.712
Present	0.3	1.114	2.756

TABLE 1. Computed drag coefficient and wake length for flow around a sphere at $Re_D = 100$.

The dynamics of the unsteady flow cases can be conveniently characterized by analysing the spectra of the drag coefficient, $c_D = 2F_x/(\rho_\infty u_\infty^2 \pi R^2)$, which are shown in figure 7 as a function of the Strouhal number based on the sphere diameter. Consistent with the findings of other authors (Mittal 1999*a*; Tomboulides & Orszag 2000), we find that in the low-Re_D end of the unsteady regime one dominant mode is present, associated with the shedding frequency of the hairpins, at $St_D \approx 0.13$. At higher Re_D one additional mode is observed at lower frequency ($St_D \approx 0.04$), which is related to a modulating effect on the vortex shedding, presumably associated with the rotation frequency of the shedding plane.

The computed mean drag coefficient and the characteristic Strouhal numbers at the various Re_D considered here are compared with data from other authors in figure 8. The drag coefficient is consistent with previous incompressible data to within a few per cent, supporting the validity of the numerical algorithm and the minor influence of compressibility in a three-dimensional flow environment. The predicted Strouhal numbers associated with the shedding and the low-frequency modes are also consistent with other studies, even though the scatter is more significant.

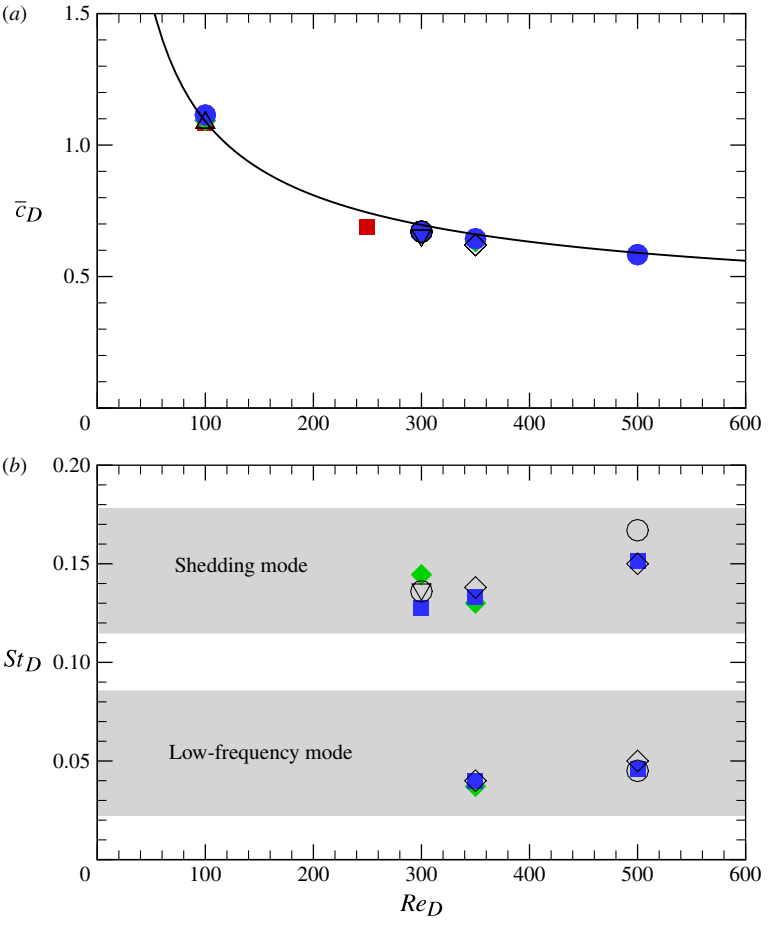

FIGURE 8. (Colour online) (*a*) Drag coefficient and (*b*) Strouhal number for flow around a sphere. Solid symbols denote our simulations at $M_\infty = 0.1$ (square), $M_\infty = 0.2$ (diamond), $M_\infty = 0.3$ (circle). Open symbols denote data from other authors: Δ, Fornberg (1988); ∇, Johnson & Patel (1999); $\diamond$, Mittal (1999*b*); $\circ$, Tomboulides & Orszag (2000). The solid line in (*a*) denotes the empirical fit $c_D = 0.28 + 6/Re_D^{1/2} + 21/Re_D$ (Wu & Faeth 1993).

4. Flow around a rolling wheel

The computational set-up used for the study is sketched in figure 9. The total length of the computational domain in the streamwise direction is $L_{x_1} + L_{x_2} = 30R$, and the axis of the wheel (which is assumed to be the origin of the reference system) is placed at $L_{x_1} = 10R$ from the inflow. The length of the domain in the spanwise and wall-normal directions is $L_z = 10R$, $L_y = 10R$, respectively. Preliminary studies have shown that the selected domain size is sufficient to minimize numerical blockage effects. To accurately mimic the case of a wheel rolling on the wall without slip, the wheel is made to rotate with angular velocity $\Omega = u_\infty/R$ (where R is the wheel radius) in the anticlockwise direction, and a translation velocity equal to the free-stream value is imparted to the bottom wall. As shown by Stewart *et al.* (2010*a*,*b*), this arrangement prevents the formation of a boundary layer upstream of the wheel, which is a major difficulty in experimental studies, in which the boundary

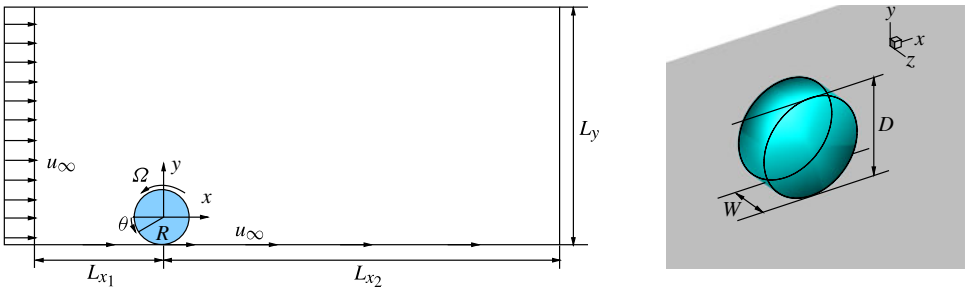

FIGURE 9. (Colour online) Sketch of computational arrangement for the study of flow around a rolling wheel.

layer issuing from the wind tunnel walls must be suitably removed through bleeding holes (Fackrell & Harvey 1975). The aspect ratio of the cylinder is taken to be $W/D = 0.4$, which is typical of racing car tyres (Fackrell & Harvey 1973). The mesh is stretched in all three coordinate directions, and the mesh spacing around the wheel is $\Delta x \approx \Delta y \approx \Delta z \approx R/60$, which, as shown later, is sufficient to resolve the boundary layer enveloping the wheel. The total number of grid points in the three coordinate directions is $768 \times 256 \times 384$.

Given the results of the simulations around a sphere, which suggest a very weak effect of compressibility in three-dimensional flow, the simulations were carried out at $M_\infty = 0.3$, to keep the computational effort within reasonable bounds. The simulations were advanced over time intervals of 10^2–$10^3 D/u_\infty$, to allow for initial transients to be washed away, and to collect a sufficiently long time record to have meaningful flow statistics. Several values of Reynolds number based on the wheel diameter were considered, namely $Re_D = 100, 200, 300, 400, 500, 1000$, to establish its influence on the flow dynamics.

An additional simulation was performed at $M_\infty = 0.1$, $Re_D = 1000$, to quantify possible effects of flow compressibility, and another one at $M_\infty = 0.3$, $Re_D = 1000$, on a grid with doubled resolution in all coordinate directions, to verify grid convergence in the most critical flow case. However, owing to the huge computational cost, this simulation was only continued until the mean flow properties were reasonably converged, and unless explicitly stated, the results reported hereafter refer to the baseline grid.

4.1. *Instantaneous fields and spectral analysis*

The qualitative properties of the flow fields can be understood from inspection of the instantaneous flow visualizations shown in figures 10–11. The vortex pattern in the wheel wake is rendered through iso-surfaces of the swirling strength, as previously done for the flow around a sphere. For $Re_D \leqslant 300$ the flow is characterized by the presence of a boundary layer around the body, which detaches from its upper edge to form an arch-shaped vortex. Two small longitudinal vortices are observed to depart from both sides of the wheel near the wall, which resemble the downstream legs of the horseshoe vortex that typically develops at the base of obstacles in developing boundary layers (Acarlar & Smith 1986). One should however note that in this case there is no boundary layer in the upstream flow, and the near-wall vorticity must be fed by the vorticity that forms around the wheel and is conveyed to the contact region

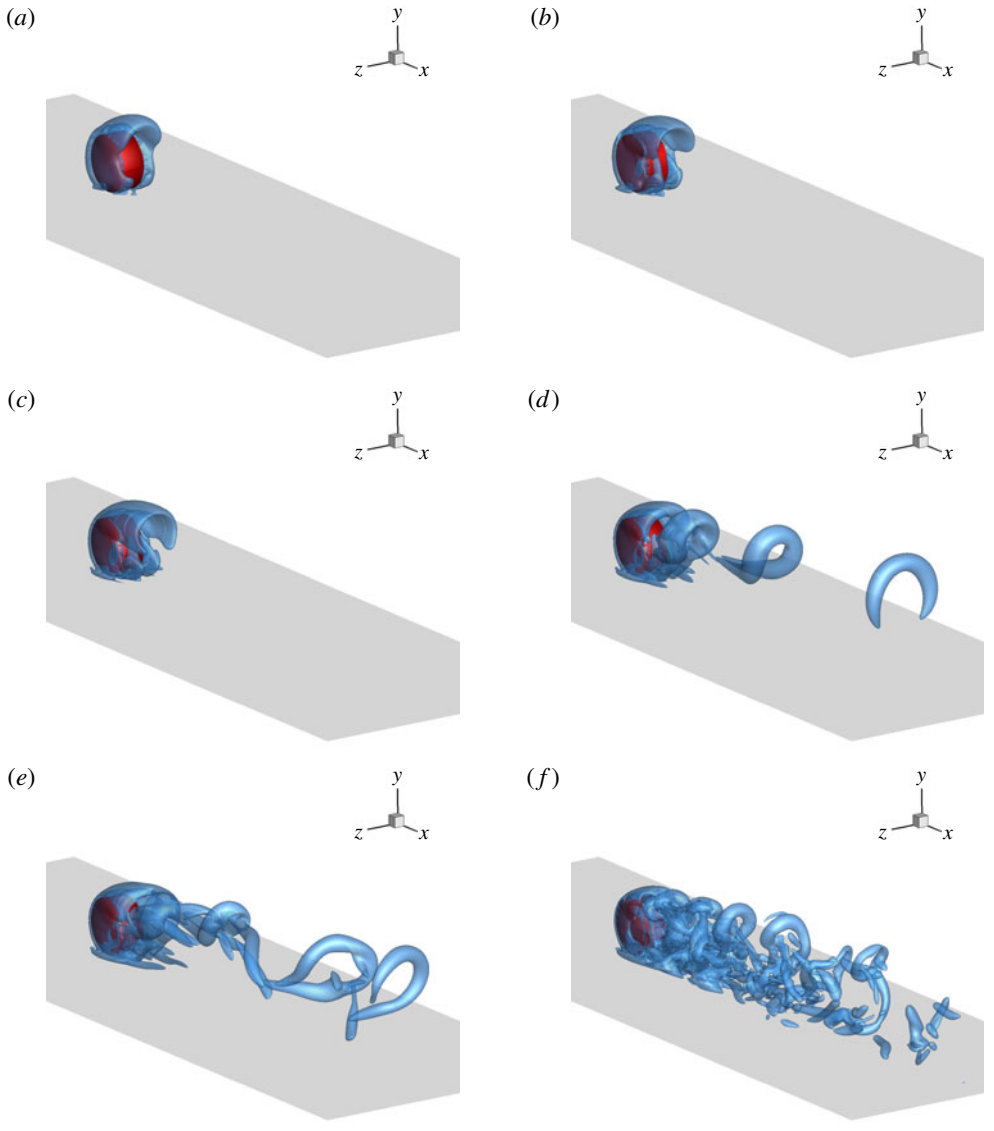

FIGURE 10. (Colour online) Vortical structures (educed through swirling strength iso-surfaces, $\lambda_{c,i} = 0.2u_\infty/D$) in the near wake of a rolling wheel at (*a*) $Re_D = 100$, (*b*) $Re_D = 200$, (*c*) $Re_D = 300$, (*d*) $Re_D = 400$, (*e*) $Re_D = 500$, (*f*) $Re_D = 1000$. Axonometric view.

by the wheel rotation. Once in the contact region, the vorticity is diverted toward the exterior of the wheel, becoming tilted in the streamwise direction.

It is noteworthy that the low-Reynolds-number simulations ($Re_D \leqslant 400$) do not exhibit any shedding of eddies in the wheel wake. Shedding of hairpin-shaped vortex tubes is observed only for $Re_D \gtrsim 400$. In this case hairpin vortices are shed in a very ordered fashion at $Re_D = 400$, in which case the flow retains perfect symmetry about the middle x–y plane. The shedding of hairpins at $Re_D = 500$ is found to be more chaotic, and planar symmetry is lost. The top view of figure 11 apparently supports the occurrence of a sinuous mode of oscillation in the wake, associated with a change

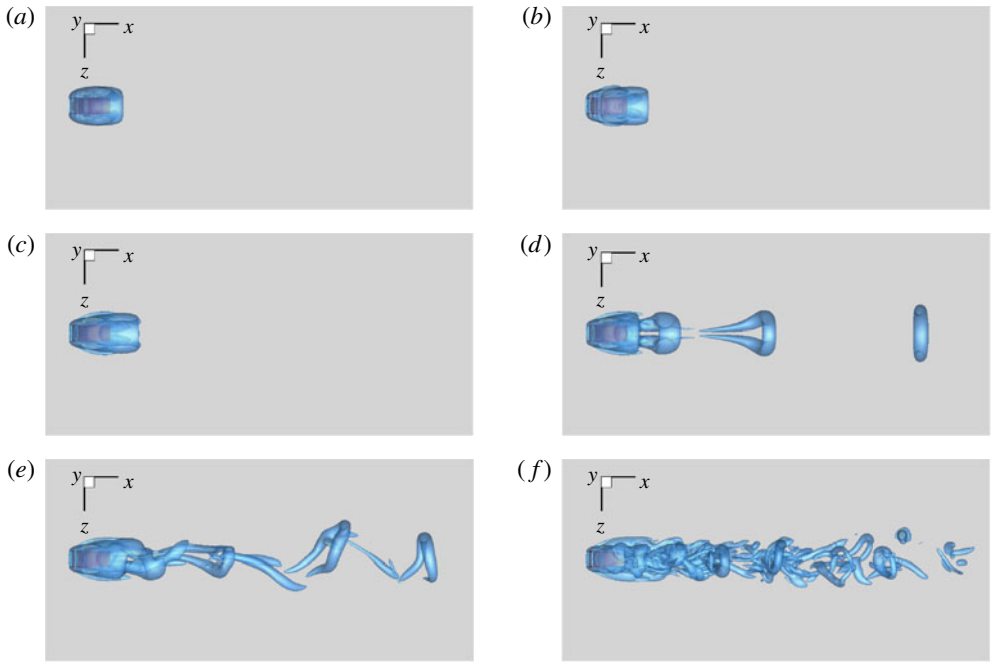

FIGURE 11. (Colour online) The same as figure 10, top view.

in the shedding direction of the hairpins from time to time. The flow becomes even more disordered at $Re_D = 1000$, even though remnants of hairpin vortices are clearly visible. In this case the presence of sinuous or varicose oscillations of the wake is harder to discern, and probably the two modes coexist. If so, the spanwise excursion of the shed eddies is more limited, compared to the $Re_D = 500$ case. It is also worth noticing that, as the Reynolds number increases, the streamwise distance between consecutive hairpins is reduced, which is consistent with the observed increase of the typical Strouhal numbers with Re_D in flows past cylinders and spheres. A similar route of transition to a chaotic state was also recently observed by Rao *et al.* (2012) in the flow past a rolling sphere.

The mechanisms of vorticity generation and transport can be clarified considering the iso-surfaces of the individual vorticity components, shown in figures 12–14. As expected, spanwise vorticity (given in figure 12) in the close proximity of the wheel surface is clockwise (i.e. positive), given the contrast between the upstream motion of the tip of the wheel and the incoming flow. A layer of positive spanwise vorticity is observed on both sides of the wheel and behind it near the wall, as a consequence of the acceleration imposed by the bottom wall on the retarded wake flow. When the Reynolds number becomes sufficiently high (figure 12*d*), part of the positive vorticity layer detaches from the contact zone, yielding downstream-leaning tongues. At $Re_D = 1000$ the positive and negative vorticity layers in the wheel wake interact, giving rise to discrete ω_z patches. In particular, the heads of the hairpin vortices are clearly visible in the upper part of figure 12(*f*). Streamwise vorticity (figure 13) is mainly produced at the upstream bottom and top edges of the wheel, because of the strong wall-normal acceleration of the fluid particles (mainly associated with the $\partial v/\partial z$ derivative). Quasi-streamwise concentrations in the wheel wake are found to be

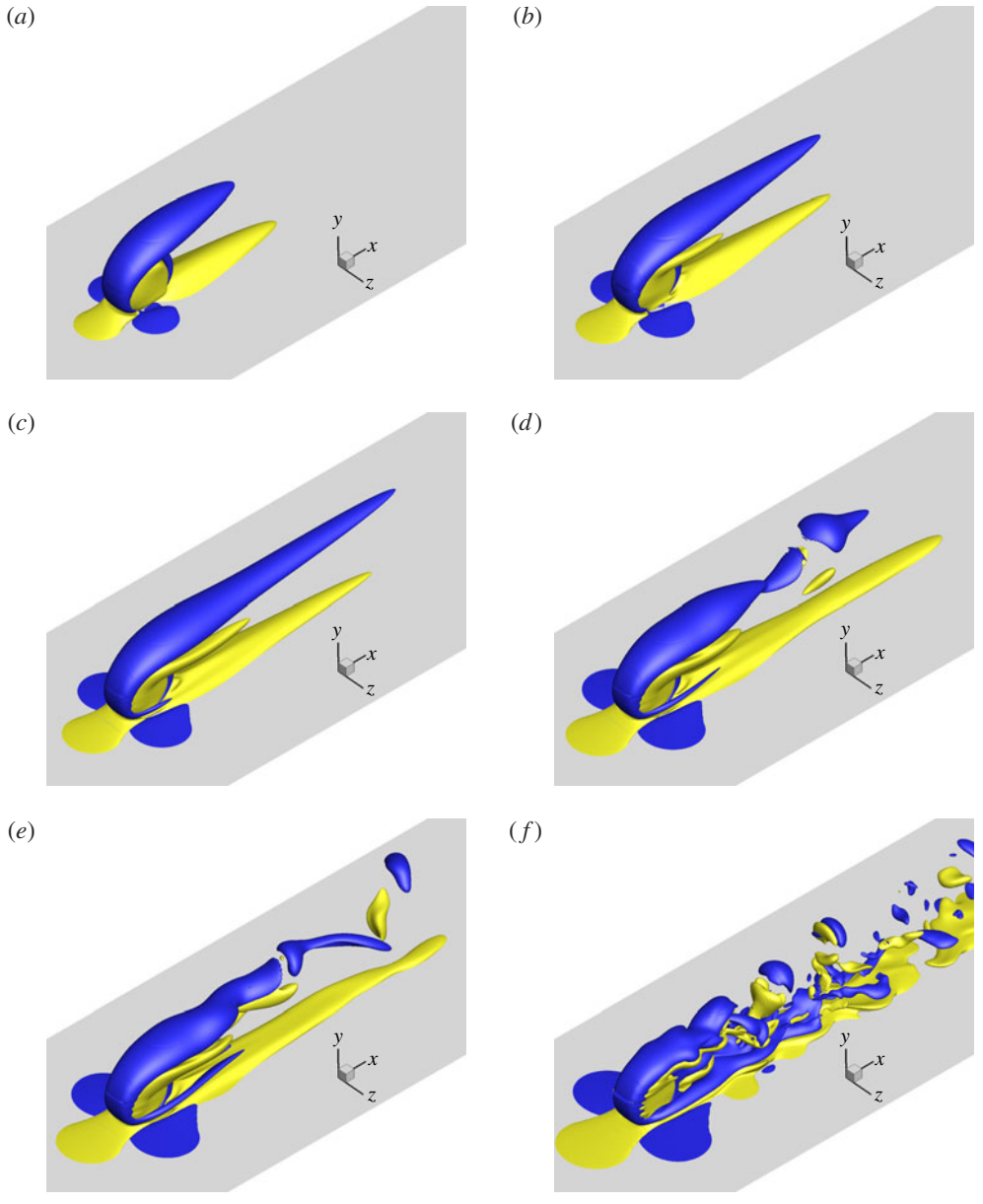

FIGURE 12. (Colour online) Iso-surfaces of spanwise vorticity, $\omega_z = \pm 0.2 u_\infty / D$ (positive in light shades, negative in dark shades), in the near wake of a rolling wheel at (*a*) $Re_D = 100$, (*b*) $Re_D = 200$, (*c*) $Re_D = 300$, (*d*) $Re_D = 400$, (*e*) $Re_D = 500$, (*f*) $Re_D = 1000$.

formed because of the roll-up of the streamwise vorticity near the contact point with the ground, whose length increases with Re_D. Streamwise vorticity tubes of different sign are seen to become intertwined in the upper part of the wake (figure 13*d–f*), and contribute to the legs of the hairpin vortices of figure 10. The wall-normal vorticity (figure 14) is mainly produced from the middle upstream edge of the wheel, where the fluid particles undergo strong acceleration in the streamwise direction, associated with

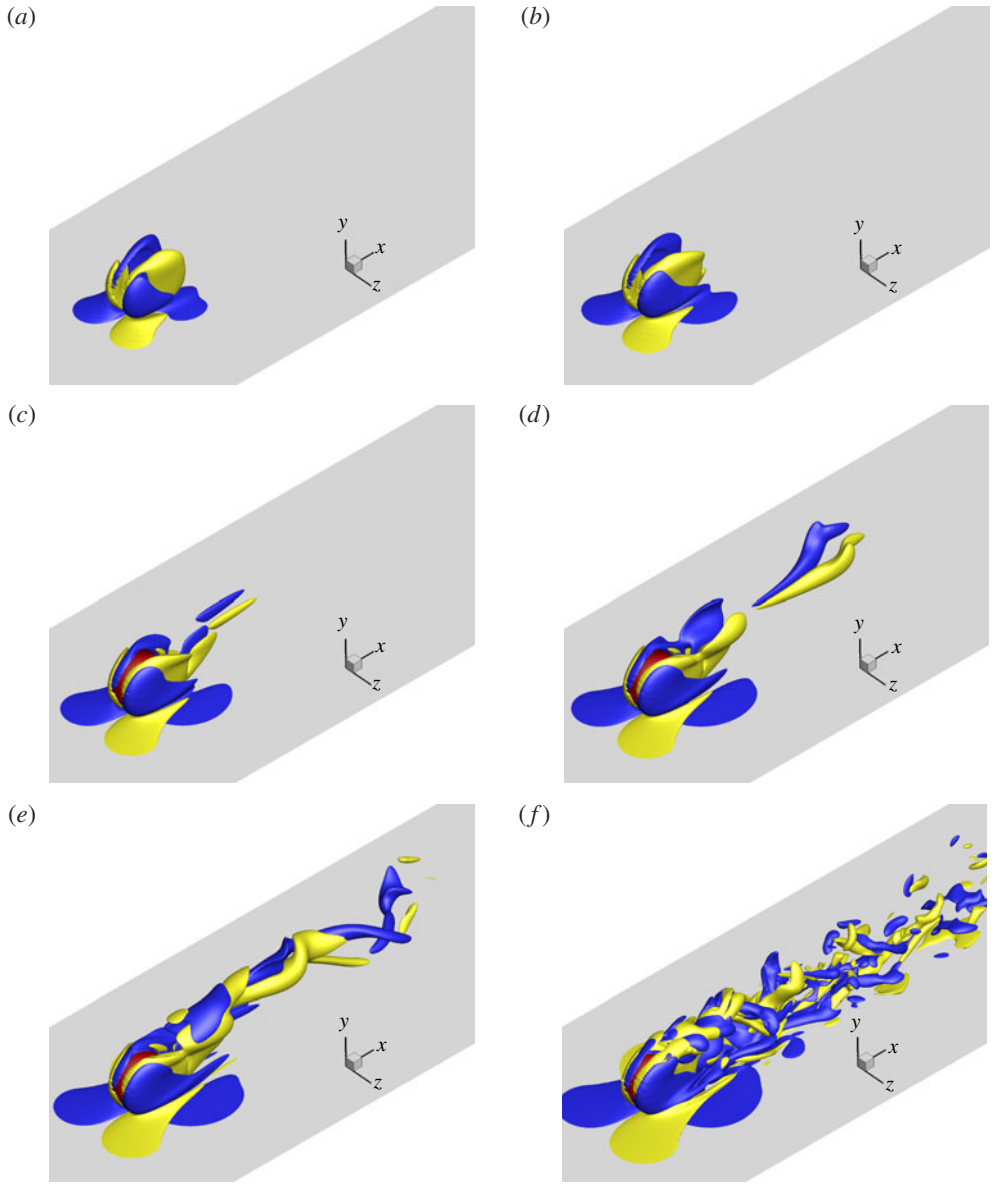

FIGURE 13. (Colour online) Iso-surfaces of streamwise vorticity, $\omega_x = \pm 0.2 u_\infty / D$ (positive in light shades, negative in dark shades), in the near wake of a rolling wheel at (*a*) $Re_D = 100$, (*b*) $Re_D = 200$, (*c*) $Re_D = 300$, (*d*) $Re_D = 400$, (*e*) $Re_D = 500$, (*f*) $Re_D = 1000$.

the $\partial w/\partial x$ derivative (but $\partial u/\partial z$ is also important). The wall-normal vorticity tends to concentrate into tube-like vortices departing from the contact region, and into large tube-like structures that detach from the upper part of the wheel, giving rise to the necks of the hairpin vortices.

The results can be quantitatively interpreted by monitoring the force coefficient experienced by the rolling wheel. Note that in this case, consistent with engineering practice, the reference area for the definition of c_D, c_L, c_Z is the cross-stream section

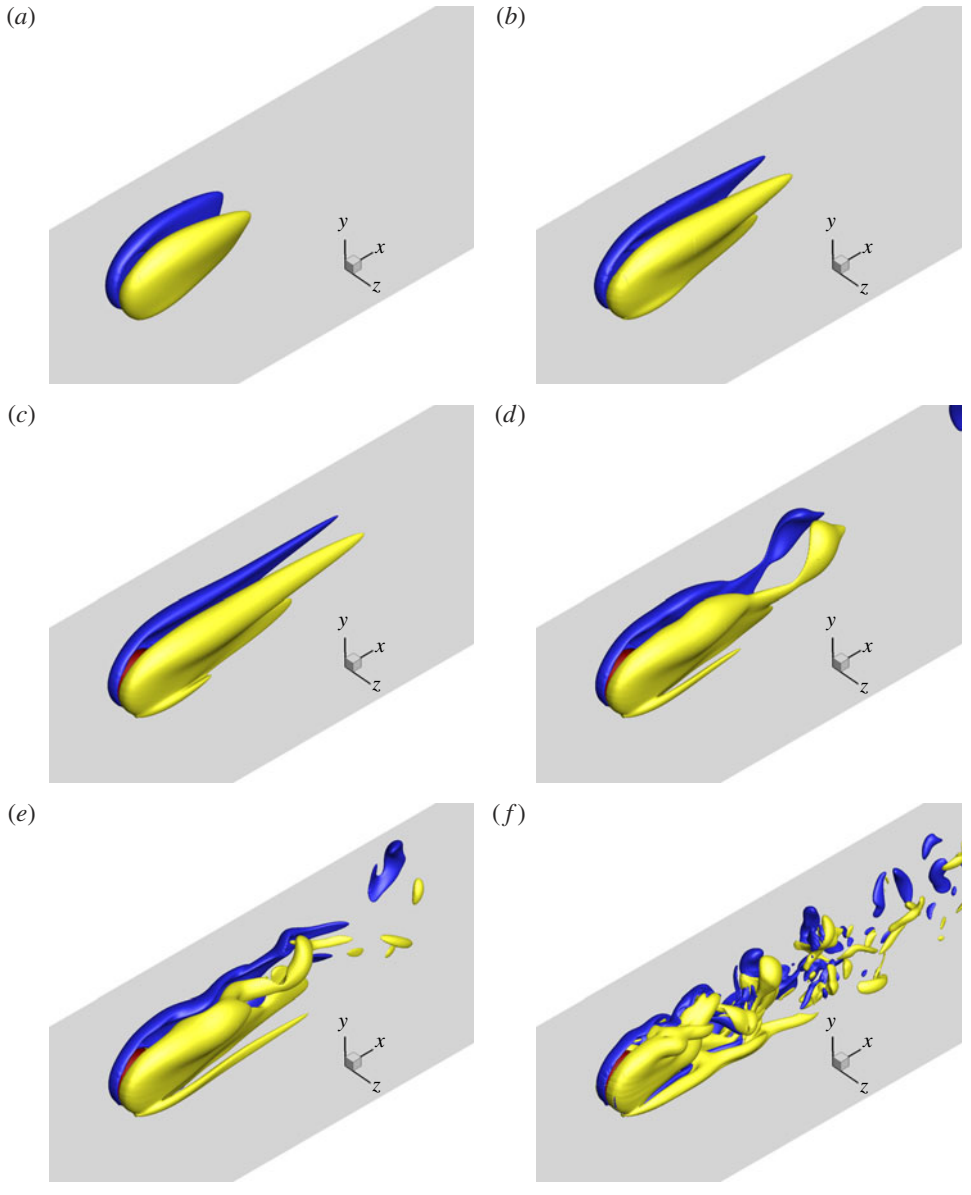

FIGURE 14. (Colour online) Iso-surfaces of wall-normal vorticity, $\omega_y = \pm 0.2 u_\infty / D$ (positive in light shades, negative in dark shades), in the near wake of a rolling wheel at (*a*) $Re_D = 100$, (*b*) $Re_D = 200$, (*c*) $Re_D = 300$, (*d*) $Re_D = 400$, (*e*) $Re_D = 500$, (*f*) $Re_D = 1000$.

of the body, $S = W \times D$. The time history of the force coefficients is displayed in figure 15, over a short time interval. Steady (or nearly steady) flow is observed for $Re_D \leqslant 300$, whereas oscillatory behaviour is found at higher Re_D, with sizeable oscillations in the side force starting at $Re_D = 500$. The mean and root-mean-square (r.m.s.) values of the force coefficients are given in table 2, and their spectral densities are plotted in figure 16, as a function of the Strouhal number. Consistent with the case of the flow around a sphere, the mean drag coefficient is found to steadily

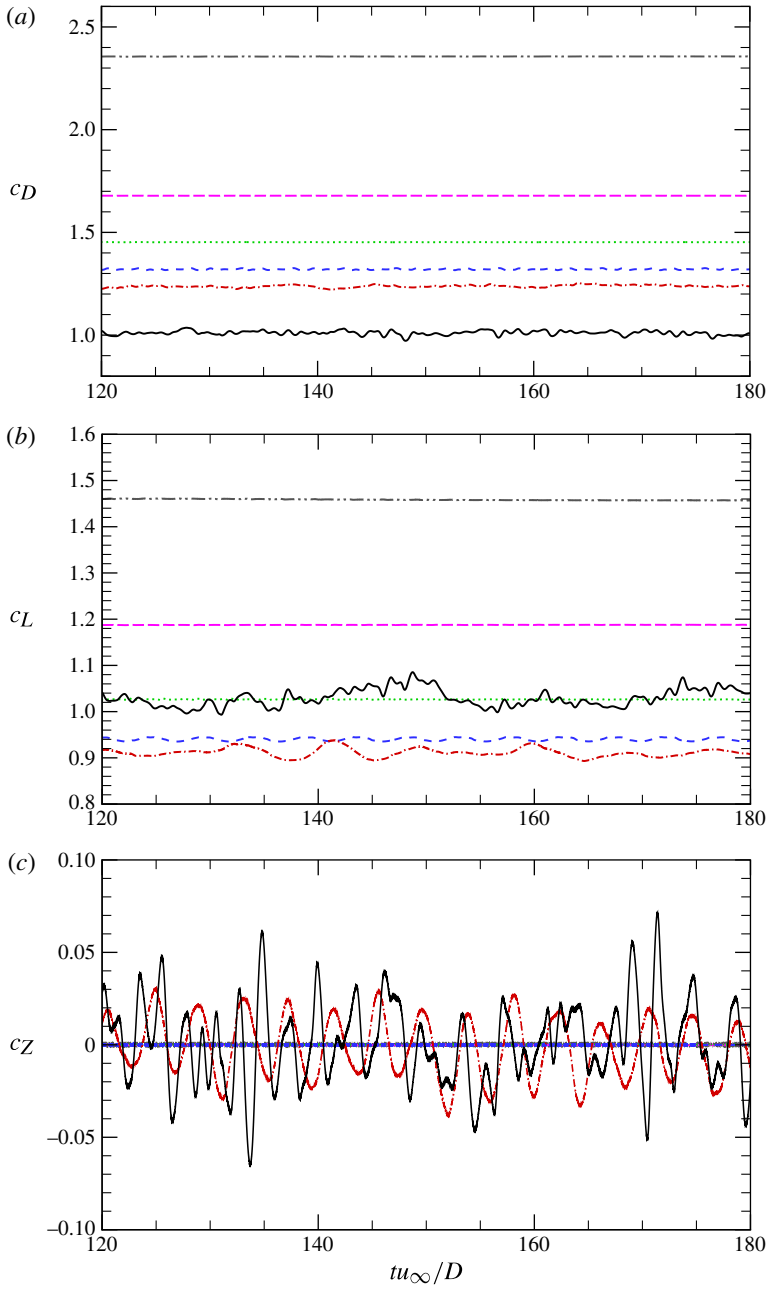

FIGURE 15. (Colour online) Time history of force coefficients for $Re_D = 100$ (dot-dot-dashed line), $Re_D = 200$ (long dashes), $Re_D = 300$ (dotted line), $Re_D = 400$ (dashed line), $Re_D = 500$ (dot-dashed line), $Re_D = 1000$ (solid line). (*a*) Drag, (*b*) lift, (*c*) side force.

decrease in the Reynolds number range considered here. In an inviscid framework, the occurrence of anticlockwise rotation of the wheel would cause a down-force, on because of the Magnus effect. In contrast, the lift coefficient is found to be positive at all Reynolds numbers. The same effect was observed by Stewart *et al.* (2010*a*,*b*)

Re_D	M_∞	$\overline{c}_D$	$\overline{c}_{D,p}$	$\overline{c}_{D,v}$	$\overline{c}_L$	$\overline{c}_{L,p}$	$\overline{c}_{L,v}$	c_{Drms}	c_{Lrms}	c_{Zrms}
100	0.3	2.35	1.76	0.59	1.44	1.62	−0.18	7.16×10^{-5}	1.25×10^{-4}	1.26×10^{-6}
200	0.3	1.68	1.41	0.27	1.19	1.34	−0.15	9.08×10^{-5}	3.37×10^{-4}	3.10×10^{-6}
300	0.3	1.45	1.30	0.15	1.03	1.16	−0.13	2.19×10^{-4}	3.79×10^{-4}	3.51×10^{-6}
400	0.3	1.32	1.23	0.09	0.94	1.07	−0.13	2.55×10^{-3}	3.36×10^{-3}	1.14×10^{-5}
500	0.3	1.24	1.19	0.05	0.91	1.03	−0.12	6.96×10^{-3}	9.86×10^{-3}	1.55×10^{-2}
1000	0.3	1.01	0.99	0.02	1.03	1.09	−0.06	1.07×10^{-2}	1.59×10^{-2}	2.39×10^{-2}
1000	0.1	1.00	0.99	0.01	1.05	1.10	−0.05	9.83×10^{-3}	1.72×10^{-2}	2.25×10^{-2}
1000*	0.3	1.05	1.00	0.01	1.01	1.07	—	—	—	—

TABLE 2. Force coefficients for flow around a rolling wheel. The subscripts p and v denote, respectively, the pressure and viscous contributions to the aerodynamic actions. All simulations are performed on a $768 \times 256 \times 384$ mesh, except the one denoted with an asterisk, which was performed on a $1536 \times 512 \times 768$ mesh.

for rolling two-dimensional cylinders and rolling spheres, and related by those authors to a strong over-pressure localized in the upstream part of the contact zone between the wheel and the ground, to which we will return when discussing figure 22. The lift force coefficient is observed to decrease up to $Re_D = 500$, and it increases again at $Re_D = 1000$. As will be shown later, this effect is linked to substantial changes in the flow topology. The side force coefficient (having zero mean for obvious symmetry reasons) has non-zero r.m.s. value for $Re_D \gtrsim 500$, reflecting the loss of symmetry observed in the flow visualizations.

The computed mean force coefficients for the simulation at $Re_D = 1000$, $M_\infty = 0.1$, shown in table 2, suggest that for the present flow conditions compressibility effects play a minor role, at least for $M_\infty \leqslant 0.3$. This is to be contrasted with the strong effect noticed for the corresponding two-dimensional simulations presented in figure 5. The force coefficients for the refined $Re_D = 1000$ simulation, also listed in the table, indicate minor grid sensitivity for the most challenging flow case. The statistics of the force coefficient fluctuations are not reported for this computation, since they were not fully converged over the time interval covered.

Further information on the nature of the aerodynamic actions can be gained by isolating the contributions of the pressure forces (indicated with the subscript p) and the viscous forces (denoted with the subscript v). For that purpose we add up the equivalent immersed boundary forces associated with the pressure and viscous terms in the Navier–Stokes equations, respectively. The results of this analysis are also listed in table 2. Regarding the drag coefficient, both pressure and viscous forces decrease as Re_D increases, but the latter at a much faster rate, becoming almost negligible at $Re_D = 1000$. A similar trend is found for the lift coefficient. The table confirms that pressure forces are responsible for the positive lift, whereas viscous forces are apparently responsible for a (small) down-force.

The spectra of the force coefficients, shown in figure 16, highlight several physical effects. At low Reynolds number ($Re_D \lesssim 300$) the flow is very nearly stationary, as can be judged by the very small value of all r.m.s. force coefficients. However, the corresponding spectra (e.g. at $Re_D = 300$), suggest the presence of (very-small-amplitude) tones at frequency multiples of about $St = 0.3$. This frequency is not related to any particular shedding mechanism, but it is linked to the rotation frequency of the wheel, which is $St_{rot} = 1/\pi \approx 0.32$. A wider band of energetically active frequencies appear in the spectrum at higher Reynolds numbers. At $Re_D = 400$ the drag and lift spectra are characterized by a strong peak at $St \approx 0.21$ (multiple

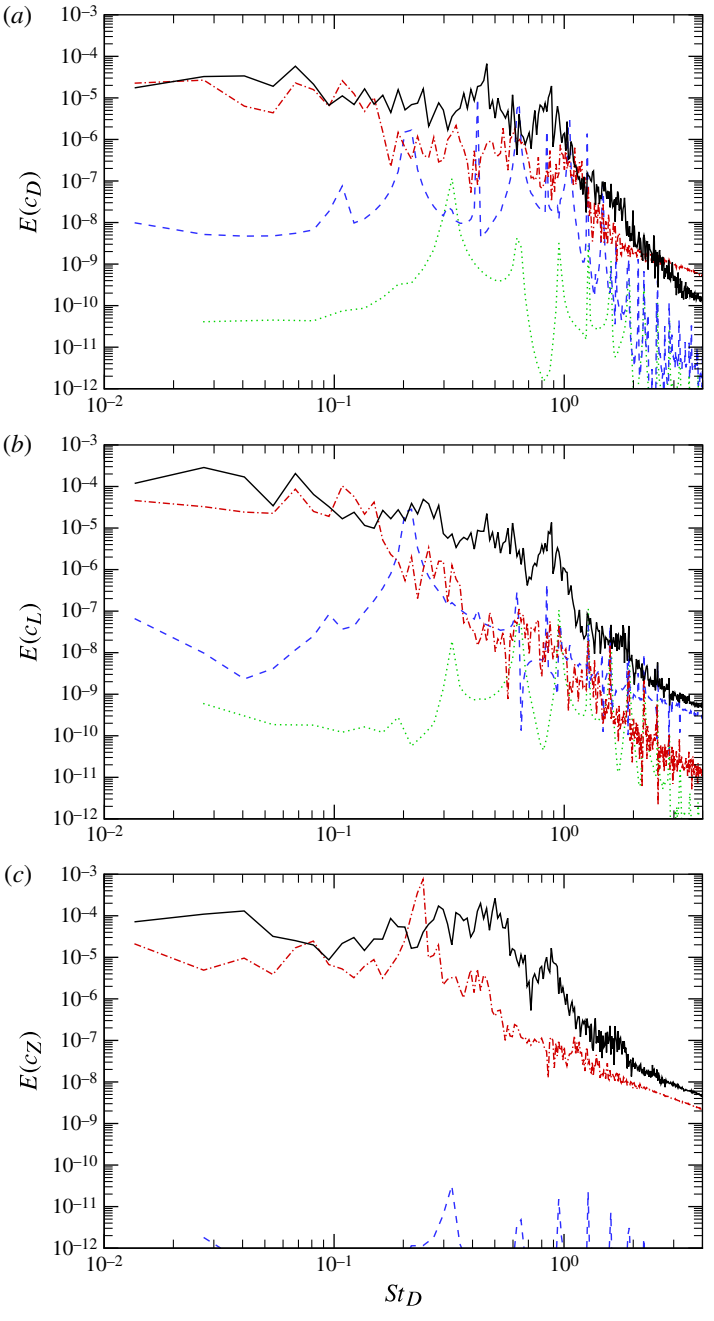

FIGURE 16. (Colour online) (*a*) Spectra of drag coefficient, (*b*) lift coefficient and (*c*) side-force coefficient for flow around a rolling wheel at $\alpha = 1$. $Re_D = 300$ (dotted line), $Re_D = 400$ (dashed line), $Re_D = 500$ (dot-dashed line), $Re_D = 1000$ (solid line).

frequencies are also apparent in the drag spectrum), and a smaller peak at $St \approx 0.1$. This value is apparently linked to the shedding frequency of the eddies in figure 10(*d*). Whenever an eddy is shed in the wheel wake, conservation of the vortex impulse

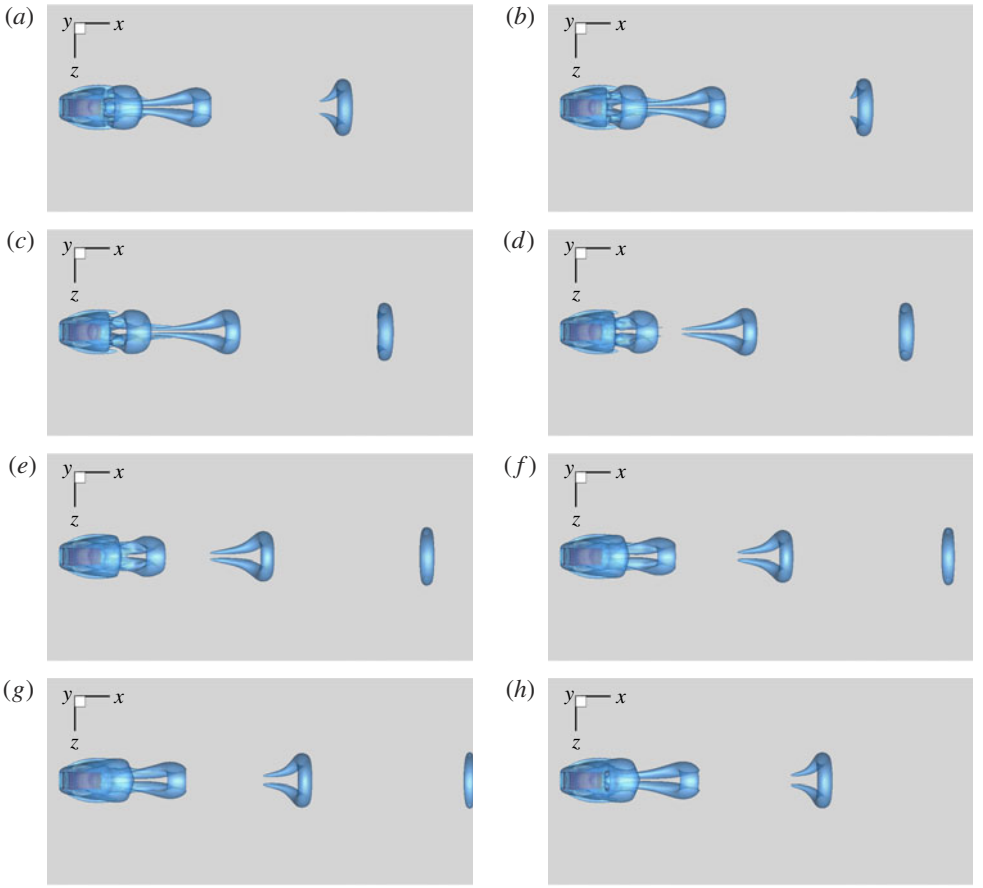

FIGURE 17. (Colour online) Vortical structures (educed through swirling strength iso-surfaces, $\lambda_{c,i} = 0.2u_\infty/D$) in the near wake of a rolling wheel at $Re_D = 400$ at various instants over one cycle of the fundamental frequency (corresponding to the bullets in figure 19*a*). Top view.

implies that a force is exerted on the wheel in the direction opposite to its motion (Jeon & Gharib 2004). To clarify this assertion, in figure 17 we show a sequence of flow snapshots at $Re_D = 400$, at equally spaced time instants, which are indicated with bullets in the time histories of the drag coefficient in figure 19(*a*). In figure 17(*a*) the primary shear layer is clearly observed on top of the wheel, and it is rolling up to give rise to a hairpin vortex. Another hairpin vortex, still connected to the shear layer through its quasi-streamwise legs, is also observed, and another one completely detached further downstream. The largest increase in the drag coefficient takes place in the time interval between figures 17(*a*) and 17(*b*), during which the new hairpin first detaches from the parent shear layer. As time progresses the hairpin proceeds downstream, until the same configuration as in figure 17(*a*) is replicated (in figure 17*h*), after which the cycle repeats itself, indicating nearly perfect flow periodicity. Focusing on the evolution of individual hairpins in the snapshots, one will also realize that the time interval between the formation of the hairpins and their final pinch-off from the wheel (taking place between figures 17*c* and 17*d*) requires

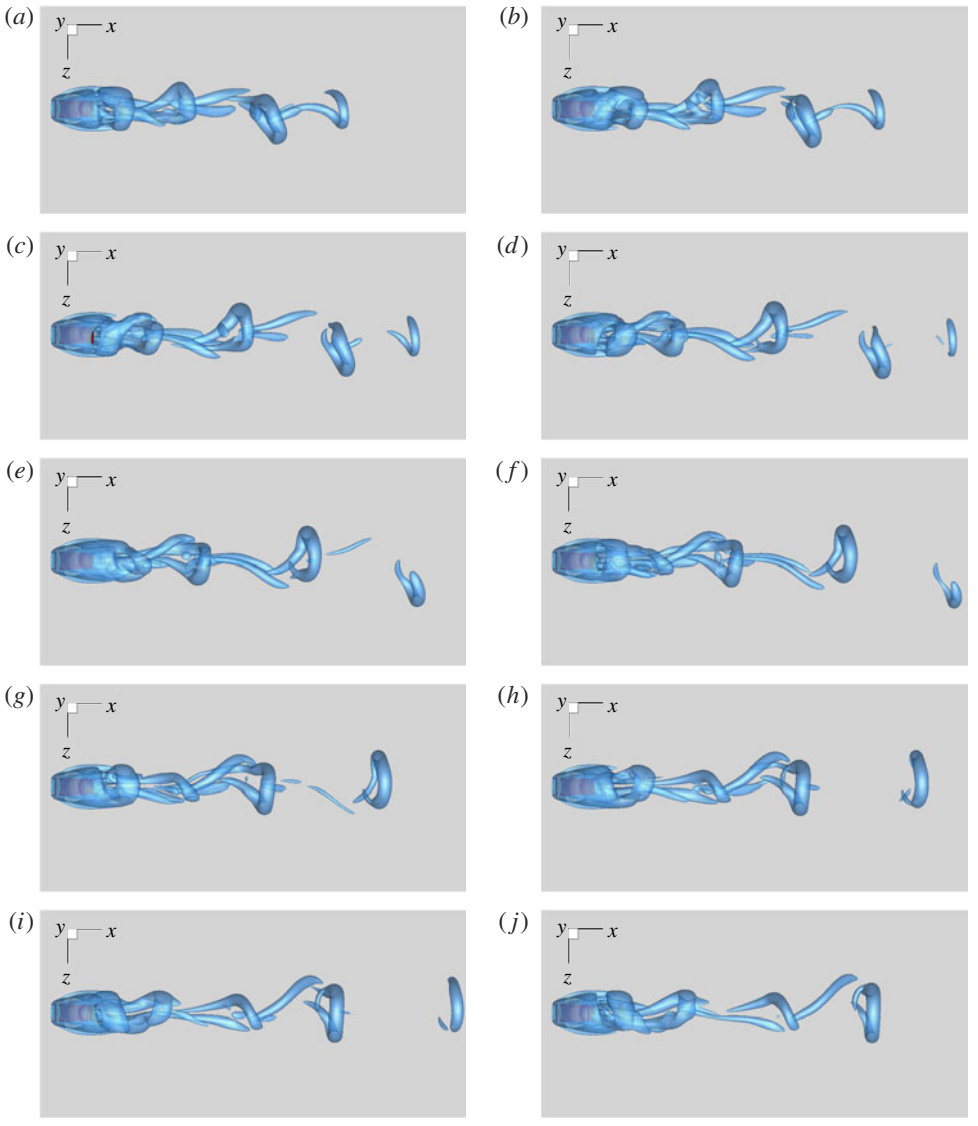

FIGURE 18. (Colour online) Vortical structures (educed through swirling strength iso-surfaces, $\lambda_{c,i} = 0.2u_\infty/D$) in the near wake of a rolling wheel at $Re_D = 500$ at various instants over one cycle of the fundamental frequency (corresponding to the bullets in figure 19*b*). Top view.

two periods of the fundamental frequency, which makes up for the weak peak in the spectra of the force coefficients at $St \approx 0.1$.

At $Re_D = 500$ a peak in the force coefficient spectra associated with the shedding of eddies is still observed around $St \approx 0.2$, in the form of a pure tone in the side force. The lift and drag signals now also exhibit substantial low-frequency content, with a weakly dominant peak at $St \approx 0.1$. These observations can be interpreted by looking at the flow snapshots of figure 18, with the aid of the drag coefficient history in figure 19(*b*). Unlike in the $Re_D = 400$ case, hairpin vortices are observed to be shed off the wheel quasi-periodically at a non-zero angle with respect to the

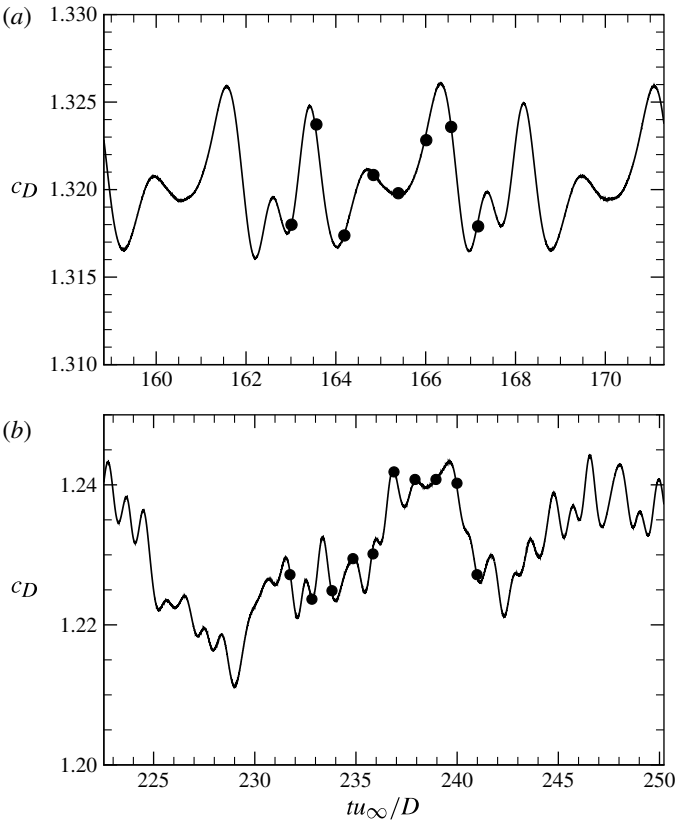

FIGURE 19. Time evolution of drag coefficient for (*a*) $Re_D = 400$ and (*b*) $Re_D = 500$. The bullets correspond to the flow snapshots shown in figures 17 and 18.

streamwise direction, yielding a tonal contribution to the side force. Focusing on the hairpin forming from the primary shear layer in figure 18(*a*), one will notice that its detachment is not perfectly symmetric with respect to the x–y plane, and as it detaches and proceeds downstream, it tends to bend in the positive-z direction. The opposite happens to the next hairpin (forming around figure 18*d*), which bends in the negative-z direction. An alternating sinuous pattern of hairpin vortices results, which very nearly repeats itself over the time interval covered in figure 18, and corresponding to one period of the low-frequency oscillation ($St \approx 0.1$). During this interval two hairpins are shed, which explains the presence of two primary peaks in the spectra of the aerodynamic coefficients. The scenario further changes at $Re_D = 1000$. At these conditions, a clear peak at $St \approx 0.2$ is only observed for the lift signal, and the spectrum in the low-frequency end is nearly flat, reflecting the onset of dynamics with very long times scales, barely resolvable with the available flow record. The spectrum for $St \gtrsim 0.2$ is found to be dense, with the formation of a nearly power-law region, which might hint at transition to a turbulent state within the wake.

4.2. *Mean fields and flow topology*

The mean structure of the wheel wake is shown in figure 20, where the same type of representation is used for the time-average fields as for the instantaneous fields of figure 10 (except for a closer viewpoint). As expected, the mean and instantaneous

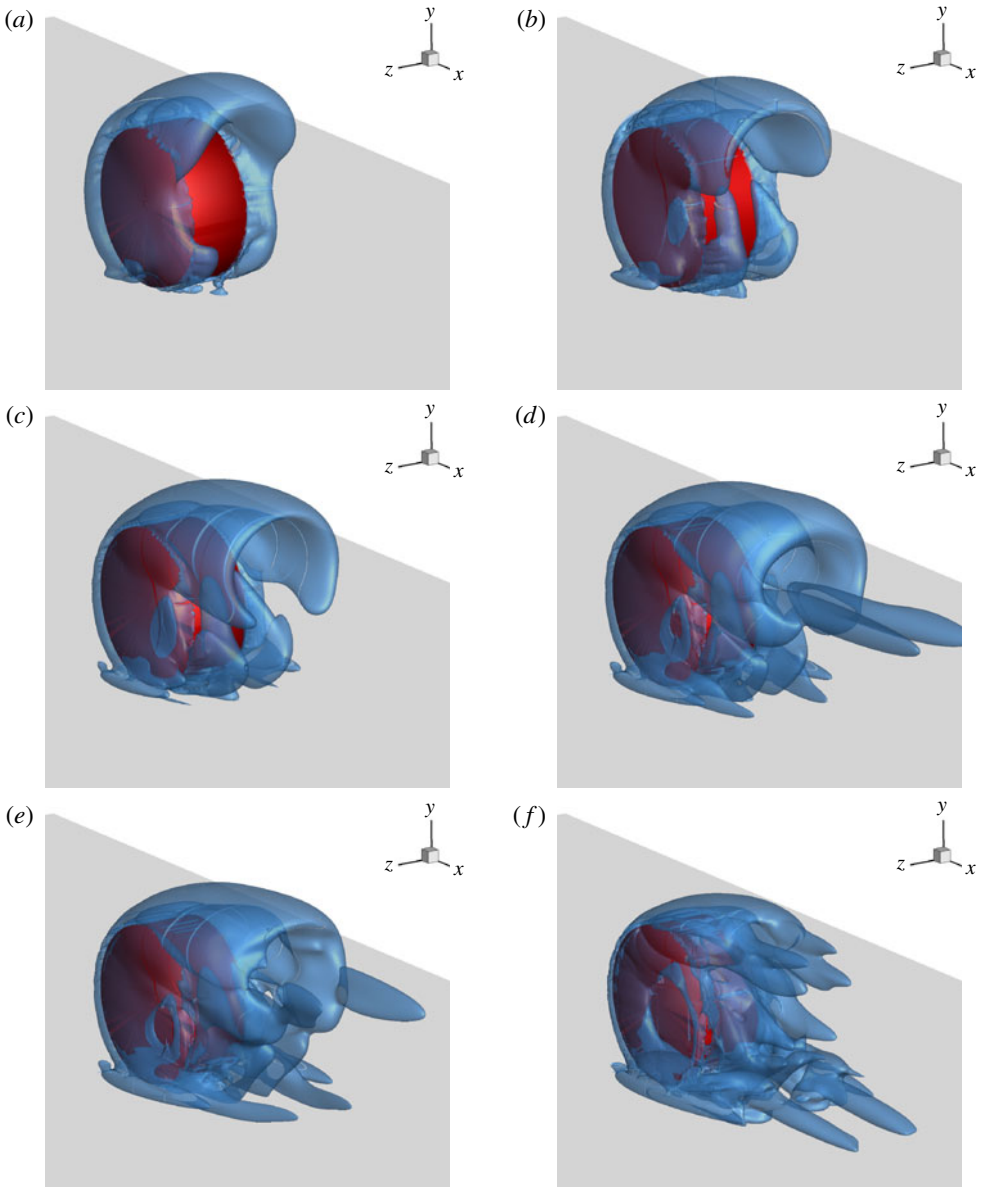

FIGURE 20. (Colour online) Time-averaged vortical structures (educed through swirling strength iso-surfaces, $\lambda_{c,i} = 0.2u_\infty/D$) in the near wake of a rolling wheel at (*a*) $Re_D = 100$, (*b*) $Re_D = 200$, (*c*) $Re_D = 300$, (*d*) $Re_D = 400$, (*e*) $Re_D = 500$, (*f*) $Re_D = 1000$. Axonometric view of the mean field.

flow visualizations do not differ visibly for $Re_D \leqslant 300$, the flow being very nearly stationary. At $Re_D = 400$, while no change is observed around the contact line and in the lower part of the wake, differences are found in the upper part of the wake, where the shedding of eddies in the instantaneous fields translates in mean flow terms into the onset of two quasi-streamwise vortex tongues. At $Re_D = 500$ similar considerations apply, but the streamwise tongues appear to be less intense, presumably

because of the averaging effect caused by the wavy spanwise motion of the wake. As the Reynolds number becomes higher ($Re_D = 1000$) the average structure of the wake changes, and three pairs of counter-rotating quasi-streamwise vortices form, one pair being the trace of the upper-wake shedding, another pair associated with the near-wall vortices (significantly intensified compared to the lower-Re_D cases), and one further pair detaching from the middle of the wheel.

In figure 21 we show the profiles of the mean tangential velocity (u_θ) in the vicinity of the wheel surface in its mid-plane, in the $\theta = 0°, 270°, 180°$, directions. The velocity profiles in the 0° direction (corresponding to the wheel's front point) show the typical behaviour of an attached laminar boundary layer, with flow pointing towards the wheel/ground contact point. As expected, the thickness of the layer decreases as Re_D becomes higher. At the upper edge of the wheel ($\theta = 270°$) the thickness of the boundary layer is much larger, and the tangential velocity exhibits a sign inversion, which is a symptom of flow separation. At this position, because of the no-slip condition the fluid particles adjacent to the body surface must move anticlockwise, following the rotation of the wheel, whereas particles further away from the surface must move in the opposite direction, following the main stream. Although the flow is fully separated in the aft part of the wheel, boundary layer behaviour is still observed at $\theta = 180°$ (figure 21*c*). It is important to note that at each of the sections under scrutiny the boundary layer thickness is larger that $0.08R$ (approximately), which implies that at least five points are placed within the boundary layer, supporting the accuracy of the flow representation.

In figure 22 we show the circumferential distribution of the mean pressure coefficient in the wheel symmetry plane, as a function of the θ angle, counted in the anticlockwise direction starting from the wheel's front point, as sketched in figure 9. Regardless of the Reynolds number, the pressure coefficient in the foremost part of the wheel is close to the unit value predicted from the inviscid theory, and lack of complete recovery is observed in the aft part, which is the cause of the large form drag. Values much larger than unity are observed near the contact point of the wheel with the ground ($\theta = 90°$). Upstream of the contact point the pressure coefficient assumes very large values, yielding a positive contribution to the overall lift, which is only partly compensated by the strong flow expansion occurring downstream of the contact point ($\theta \gtrsim 90°$). This behaviour can be interpreted as the consequence of the severe thinning that the boundary layer developing on the front part of the wheel must undergo while it is convected towards the contact point. As can be expected on the basis of figure 21(*a*), this effect is stronger the thicker is the upstream boundary layer (i.e. the lower is Re_D), and as a matter of fact the compression and the expansion taking place near the contact point become weaker as Re_D becomes higher.

The topology of the mean flow is studied next through inspection of two-dimensional slices, which are shown in figures 23–28. In the figures we plot the pseudo-streamtraces associated with the plane-restricted velocity field, whose interpretation requires some attention (Tobak & Peake 1982; Délery 2001). The pseudo-streamtraces in the x–y symmetry plane (i.e. the streamtraces formed with the $\boldsymbol{u}$–$\boldsymbol{v}$ velocity vectors), given in figure 23, highlight the presence of a primary, two-dimensional-like separation at $\theta \approx 285°$, on the right upstream side of the wheel upper edge. As noted by Fackrell & Harvey (1975), the definition of separation from a rotating object is a sensitive topic, as it cannot be directly related to the formation of a half-saddle point on its surface, as is the case of separation from a stationary object (Tobak & Peake 1982). In the present case, separation from the body surface can be linked to the presence of a saddle point within the flow, just outside the boundary layer, and which is indicated with S_1 in figure 25(*a*). Notably, the main

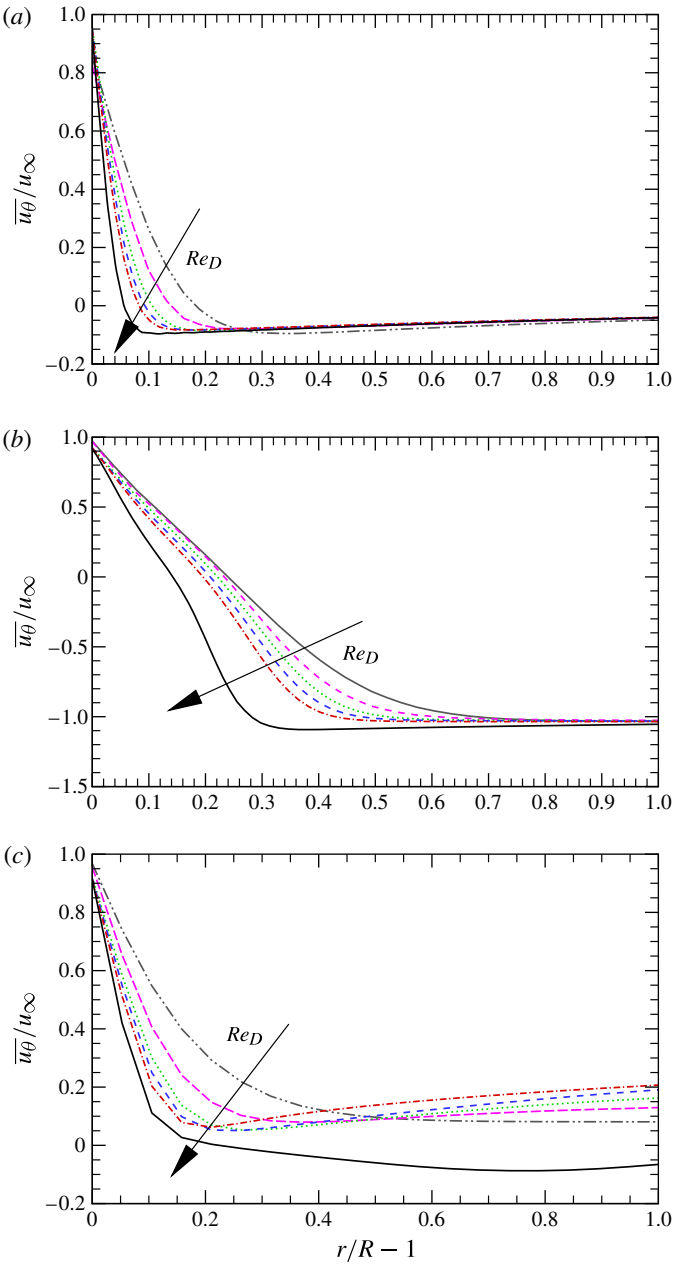

FIGURE 21. (Colour online) Time-averaged azimuthal velocity profiles near the wheel mid-plane (refer to figure 9), as a function of the wall distance, taken at (*a*) $\theta = 0°$, (*b*) $\theta = 270°$, (*c*) $\theta = 180°$. Data are shown for $Re_D = 100$ (dot-dot-dashed line), $Re_D = 200$ (long dashes), $Re_D = 300$ (dotted line), $Re_D = 400$ (dashed line), $Re_D = 500$ (dot-dashed line), $Re_D = 1000$ (solid line).

separation point is apparently unaffected by the variation of Re_D and, even in the case when the boundary layer on the wheel surface is turbulent, separation is still observed at $\theta \approx 280°$ (Fackrell & Harvey 1975).

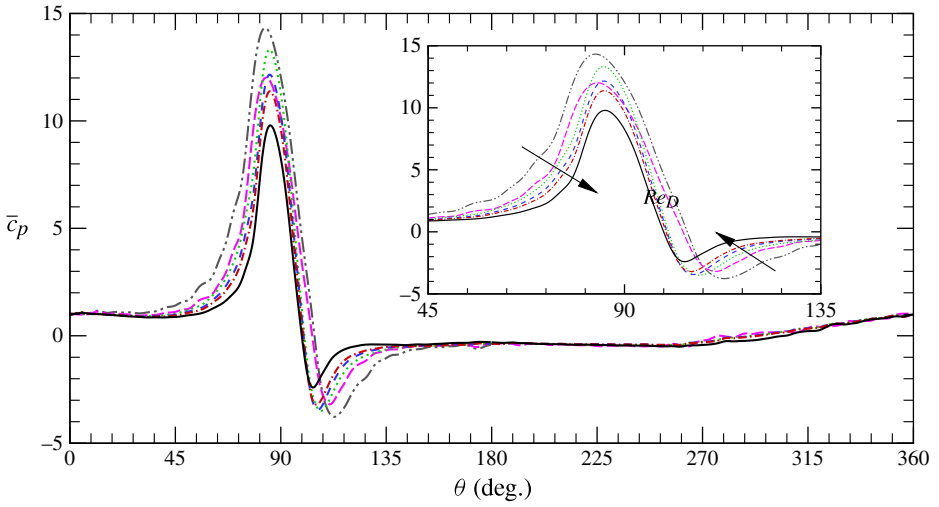

FIGURE 22. (Colour online) Time-averaged pressure coefficient at the wheel mid-plane as a function of θ (as defined in figure 9), for $Re_D = 100$ (dot-dot-dashed line), $Re_D = 200$ (long dashes), $Re_D = 300$ (dotted line), $Re_D = 400$ (dashed line), $Re_D = 500$ (dot-dashed line), $Re_D = 1000$ (solid line). The inset figure is a magnified view of the contact region.

The geometry of the streamtraces in the wheel wake for $Re_D \lesssim 300$ is characterized by the presence of a main separating streamline D_1 issuing from the primary saddle point S_1, and a weak secondary focus near the rear contact point with the ground (F_1), with an associated saddle point (S_2), as shown in the magnified view of figure 25(b). A three-dimensional reattachment line (R_1) characterized by divergence of the pseudo-streamlines, departs from F_1, which can be regarded as the downstream boundary of the separated flow region. As Re_D is increased the wake becomes longer, until a first topological change takes place at $Re_D = 400$, in which case two additional critical points appear. Specifically, a focus (F_2) with outward spiralling motion is found, which can be physically traced back to the vortex shedding activity, and which is isolated from the outer flow by an additional saddle point, which we mark as S_3. At higher Reynolds numbers ($Re_D = 1000$) a second topological change is observed, with the formation of a node of attachment type in the near wake (N), characterized by divergence of the pseudo-streamtraces, and of a further saddle point, S_4. This change implies the splitting of the separated flow region into two parts, divided by a secondary dividing streamline (D_2), which roughly coincides with the $y = 0$ line. Three-dimensional reattachment is observed at the downstream end of the lower (R_1) and the upper (R_2) parts of the separated flow region. Regarding the focus associated with the main flow separation (F_2), it is found to become smaller and to get closer to the upper edge of the wheel. In addition to these major topological changes, significant shortening of the separated flow region is observed, compared to the lower-Re cases, which is likely to be the cause for the decreased value of the pressure drag.

The streamline pattern in the symmetry plane is also reported for the $Re_D = 1000$ case at $M_\infty = 0.1$ and at $M_\infty = 0.3$ on the refined mesh in figure 24. Apparently, the flow field is not significantly affected by compressibility effects, or contaminated by insufficient mesh resolution. Therefore, we believe that observed abrupt change in the wake topology is not a result of computational artifacts. It is also noteworthy that

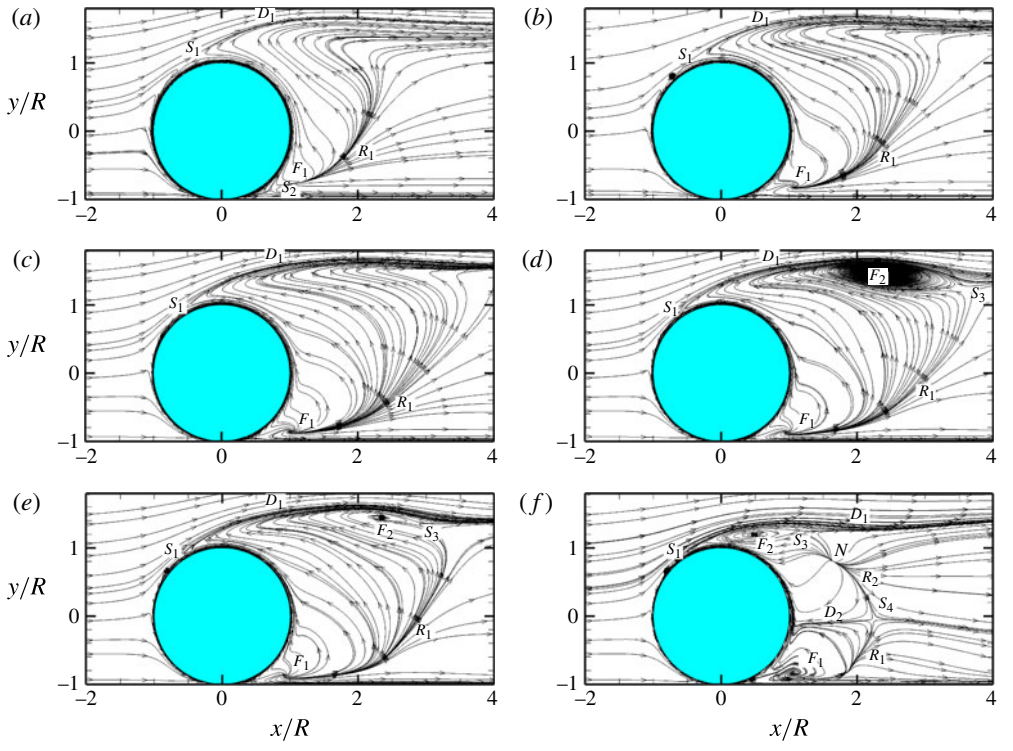

FIGURE 23. (Colour online) Time-averaged streamtraces in the symmetry plane of a rolling wheel at (*a*) $Re_D = 100$, (*b*) $Re_D = 200$, (*c*) $Re_D = 300$, (*d*) $Re_D = 400$, (*e*) $Re_D = 500$, (*f*) $Re_D = 1000$.

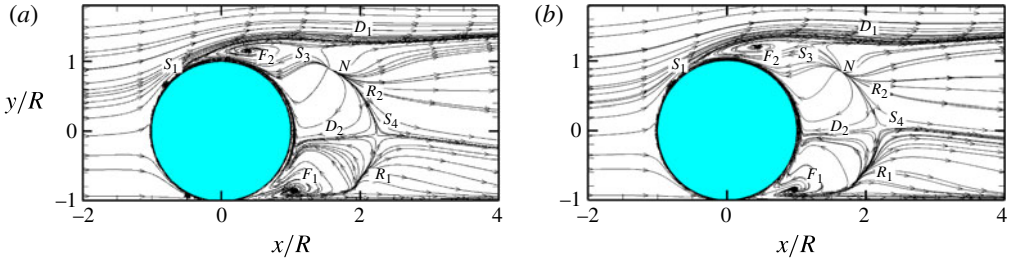

FIGURE 24. (Colour online) Time-averaged streamtraces in the symmetry plane of a rolling wheel at $Re_D = 1000$ at (*a*) $M_\infty = 0.1$ on the baseline mesh, and (*b*) $M_\infty = 0.3$ on the refined mesh. Compare with figure 23(*f*).

a very similar flow pattern to the $Re_D = 1000$ case was also observed by means of PIV visualizations in the *x*–*y* plane in experiments at much higher Reynolds numbers (Issakhanian *et al.* 2010).

When viewed in the *x*–*z* plane through the centre of the wheel (figure 26), the pseudo-streamline pattern resembles that found in two-dimensional flow around a rectangle, with a weak separation past the leading edge of the wheel, for $Re_D < 1000$, and flow separation in its wake, with nearly closed streamlines, which are indicative

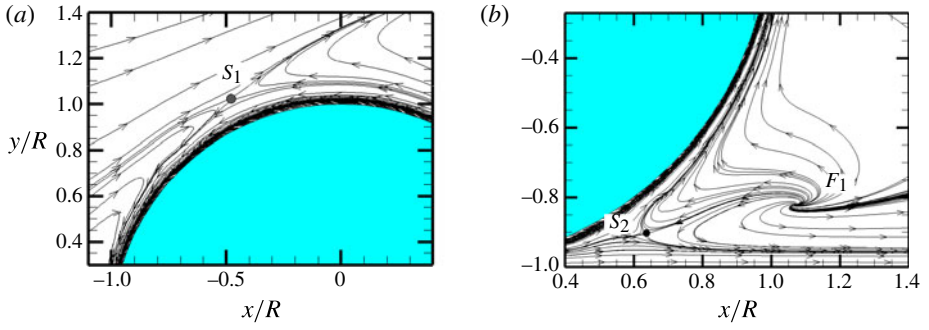

FIGURE 25. (Colour online) Time-averaged streamtraces in the symmetry plane of a rolling wheel at $Re_D = 200$. Magnified views are shown (*a*) in the vicinity of the forebody separation point and (*b*) in the aft part of the contact region.

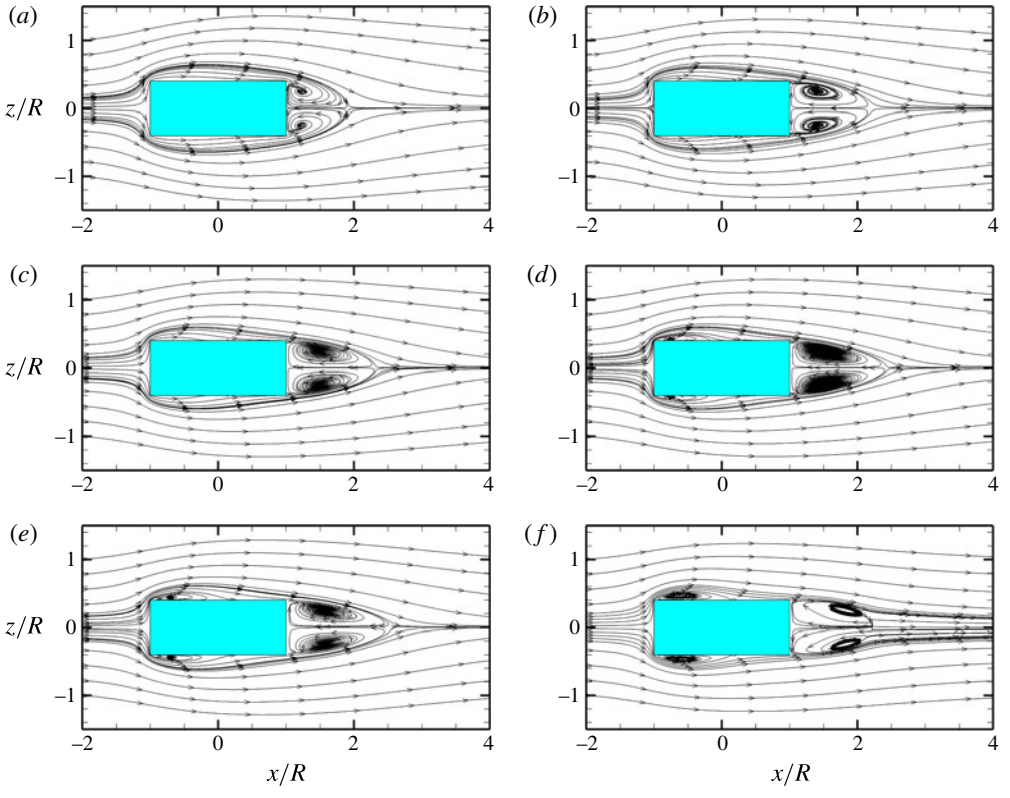

FIGURE 26. (Colour online) Time-averaged streamtraces in the $y = 0$ plane of a rolling wheel at (*a*) $Re_D = 100$, (*b*) $Re_D = 200$, (*c*) $Re_D = 300$, (*d*) $Re_D = 400$, (*e*) $Re_D = 500$, (*f*) $Re_D = 1000$.

of quasi-two-dimensional flow. At $Re_D = 1000$ the same pattern as for the other cases is observed in the lower part of the recirculation bubble (figure 27*a*), with the dominance of two counter-rotating eddies. In the upper part of the recirculation bubble

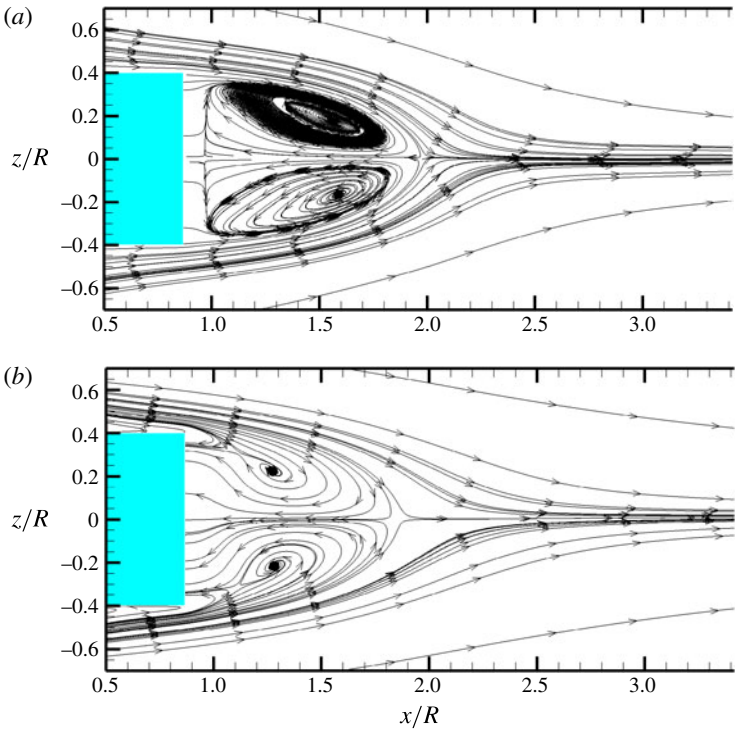

FIGURE 27. (Colour online) Time-averaged streamtraces in the wake of a rolling wheel at $Re_D = 1000$: sections at (*a*) $y = -0.5$, (*b*) $y = 0.5$.

(figure 27*b*), two small foci of separation type (Tobak & Peake 1982) are found, with an associated pair of saddle points within the flow.

The streamwise velocity fields (with superposed instantaneous streamtraces) in a cross-stream plane in the wheel wake (figure 28) show that most of the velocity deficit at low Re_D is concentrated in the upper part of the wheel, and the velocity contours have a distinctive inverse teardrop shape. As Re_D increases, the velocity deficit in the upper part of the wake is recovered within a shorter distance, owing to the chaotic shedding of hairpin vortices. On the other hand, a stronger velocity deficit is observed at the two sides of the wheel near the ground. As can be argued from inspection of the z–y pseudo-streamtraces, this phenomenon is strictly related to the intensification of the two near-wall quasi-streamwise vortices, which tend to bring low-momentum fluid from the wake interior to the periphery of the wheel. The same inverse-T shape of the velocity deficit found in figure 28(*f*) was also observed via PIV by Saddington *et al.* (2007).

Looking more in detail at the streamtrace pattern at $Re_D = 1000$, it is possible to compare with previous studies that addressed the structure of the trailing vortices past a rolling wheel, for which various models were proposed (Cogotti 1983; Saddington *et al.* 2007). Our observations support a pattern consisting of (at least) three pairs of counter-rotating vortices (also recall figure 20 for a three-dimensional representation), which we explain as follows. The edge vortices, which depart from the apex of the wheel, are associated with the roll-up of the primary separating shear layer. Their sense of rotation can be predicted by noticing that a stagnation point is present on

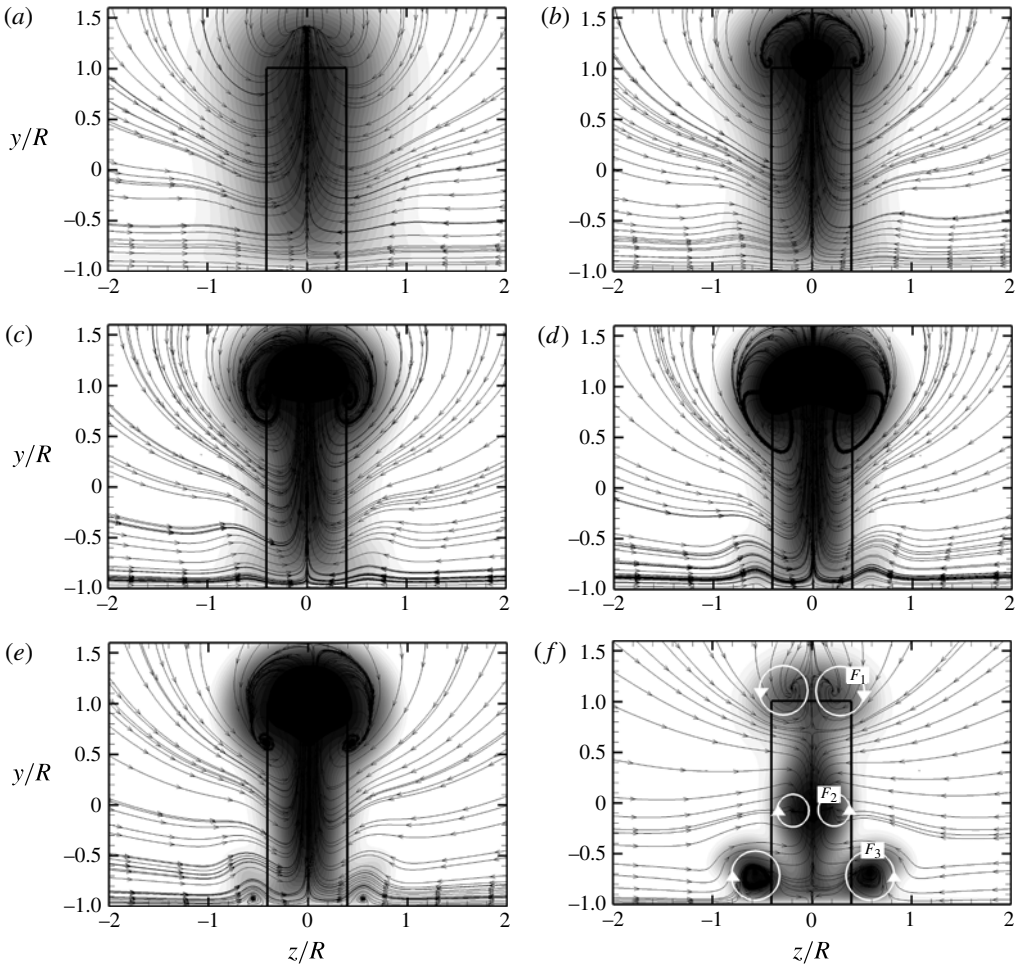

FIGURE 28. Time-averaged streamtraces and streamwise velocity contours in the cross-stream plane ($x/R = 2$) in the near wake of a rolling wheel at (*a*) $Re_D = 100$, (*b*) $Re_D = 200$, (*c*) $Re_D = 300$, (*d*) $Re_D = 400$, (*e*) $Re_D = 500$, (*f*) $Re_D = 1000$. Dark shades correspond to low speed, and light shades to high speed.

the front part of the wheel, as shown in figure 25(*a*), where the pressure is higher than around the wheel. As a consequence, the edge vortices are such as to induce an up-lift in between. In contrast, the ground vortices are formed because of the large pressure unbalance between the front and the aft part of the contact zone, and their sense of rotation is analogous to the free vortex system behind a lifting wing. The increased strength of the ground vortices with Re_D would then provide an explanation for the previously noticed tendency for the lift coefficient to rise up at $Re_D = 1000$. An additional pair of vortices is observed at $Re_D = 1000$, detaching approximately from the middle of the tyre. This vortex pair is apparently the result of the roll-up of the dividing surface that separates the lower from the upper part of the wake, and in previous experimental studies of flow around tyres it was attributed to the presence of a hub (Cogotti 1983). Extrapolating the present low-*Re* results to higher *Re*, one

would then expect that only two vortex pairs should be present in the near wake of a wheel, namely the ground and the mid vortex, whereas the edge vortex would become comparatively weaker. In that case, the same scenario would be recovered as in experiments (Saddington *et al.* 2007; Issakhanian *et al.* 2010) at $Re_D \approx 5 \times 10^5$.

Although two-dimensional sections of the flow field can give a rough idea of the flow behaviour, its complexity can be guessed (even though the interpretation is not easy from printed images) from the analysis of the three-dimensional streamtraces depicted in figure 29. At $Re_D = 500$, the streamtraces coming from the main stream are mostly diverted either on top or on the sides of the wheel. The streamtraces issued from points in the near wake tend to linger in the lower rear part of the wheel, whence they are lifted upward, and either proceed downstream in the upper part of the shear layer, or are diverted to the wheel sides, undergoing a complex rotatory motion, and eventually being absorbed again in the separated flow region, or proceeding downstream. A similar scenario is also observed at $Re_D = 1000$. However, in this case, some of the streamtraces issued from the base flow region move toward the ground, and directly proceed downstream. Some others are lifted upwards, becoming entrapped in the two vortices that dominate the upper recirculation region, and whose traces were seen in figure 27(*c*).

Even though the flow is not strictly turbulent, it is also instructive to look at the statistics of the velocity fluctuations which are shown in figure 30, limited to cases where significant unsteadiness is observed ($Re_D \geqslant 400$). Comparing with figure 23(*a–c*), one will see that most turbulent activity takes place right past the saddle point (S_3) which terminates the recirculation zone, and which moves closer to the wheel as Re_D increases. At the highest Reynolds number, significant turbulent activity also takes place past the saddle point S_4. Consistent with the universal behaviour of turbulent shear flows, the shear stress is negative in the primary separating shear layer. At $Re_D = 1000$ the turbulent shear stress also attains positive values in the region between the lower and upper recirculation bubble, where the flow has reversed direction, i.e. pointing toward the wheel. The similarity between the pattern shown in figure 23(*c*) and the experiments of Issakhanian *et al.* (2010) (see their figure 11) in this respect is striking.

5. Conclusions

We have studied the flow around a rolling wheel at low Reynolds number by means of direct numerical simulations, whereby the geometric complexity of the problem is handled through the immersed boundary method. Preliminary studies have shown the suitability of the numerical algorithm to predict the flow topology and the force coefficients for canonical two- and three-dimensional flows, including the flow around a sphere, for which large amount of information is available.

In the Reynolds number range considered here the flow around the rolling wheel exhibits the formation of a strong shear layer at the upper edge of the wheel, caused by the detachment of the boundary layer, and which becomes unstable for $Re_D \gtrsim 400$, yielding a characteristic pattern of hairpin-shaped vortices, which dominate the wake in the higher range of Re_D considered here. From a dynamic standpoint the main feature of the flow is the presence of a strong over-pressure in the fore part of the wheel near the ground, which is caused by the wall impingement of the boundary layer dragged by the wheel's front surface. A negative pressure coefficient is observed right behind the contact point with the ground, which does not compensate the strong fore compression. This observation appears to hold true in the range of low Mach

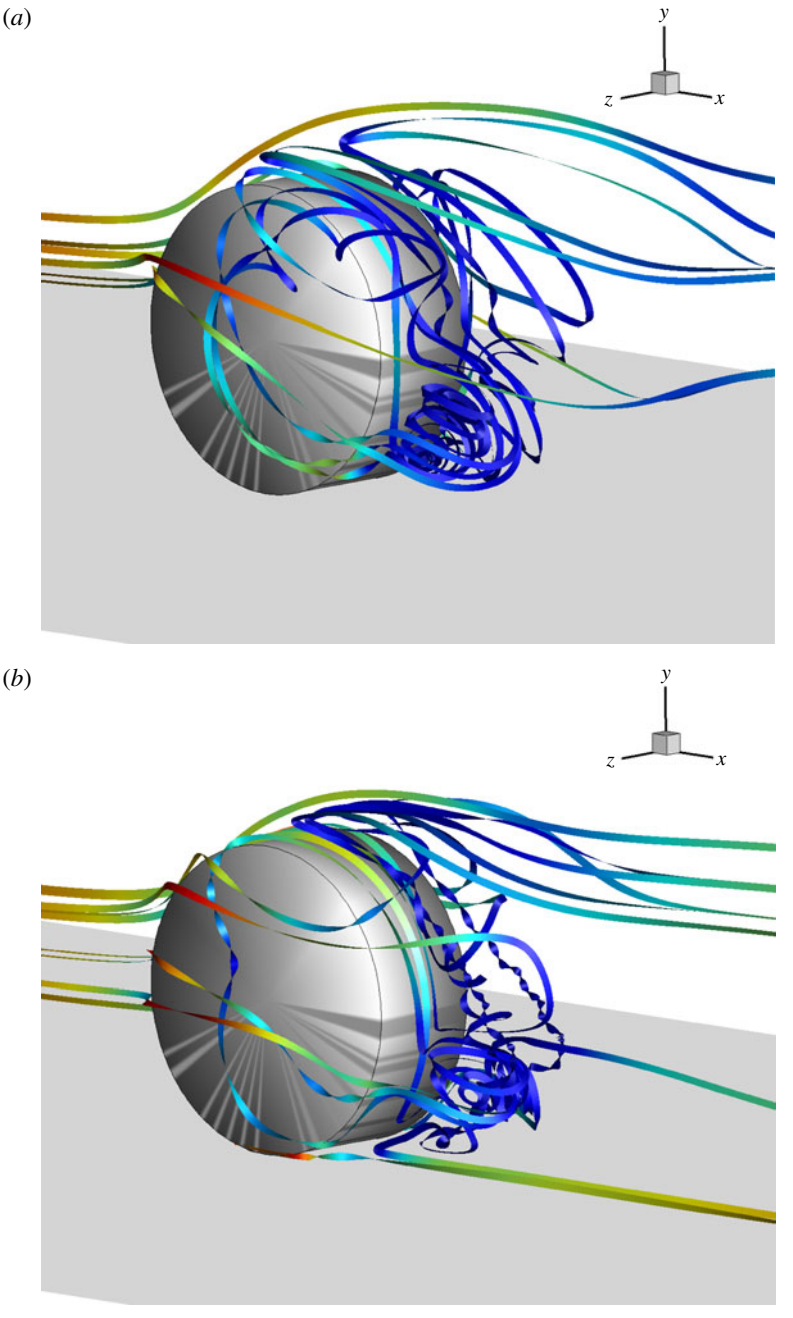

FIGURE 29. (Colour online) Time-averaged three-dimensional streamlines in the wheel wake at (*a*) $Re_D = 500$, (*b*) $Re_D = 1000$.

numbers ($M_\infty \leqslant 0.3$) and low Reynolds numbers ($Re_D \leqslant 1000$) considered here, and supports experimental studies (Fackrell & Harvey 1975) claiming that a rolling wheel produces positive lift, whereas other studies supported down-lift (Morelli 1969). Of course, given the wide disparity of Reynolds numbers (which are well in excess

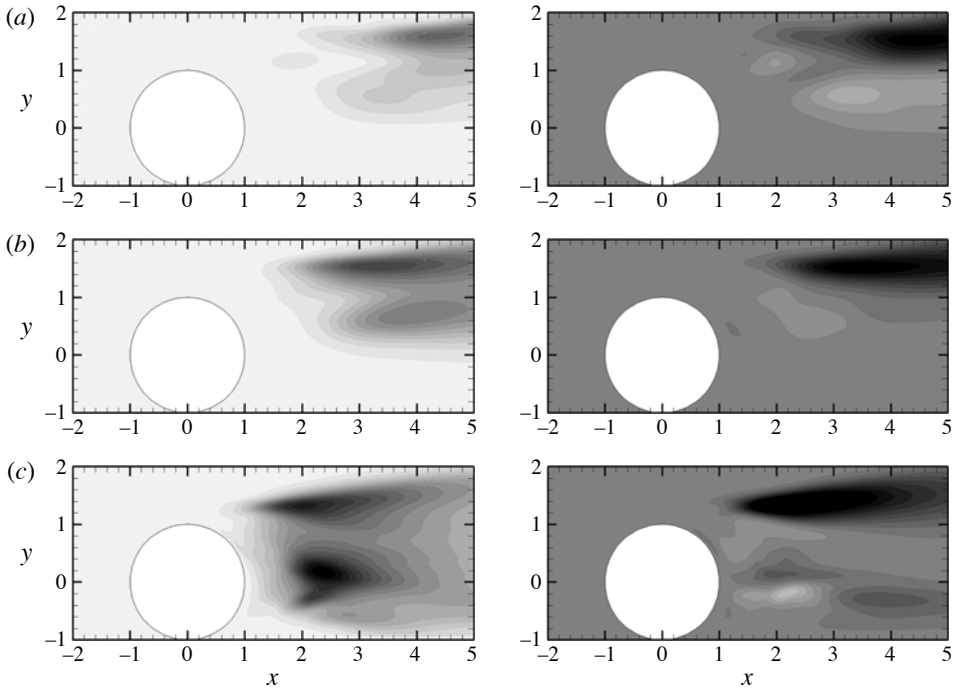

FIGURE 30. Contours of kinetic energy (left column) and Reynolds shear stress (right column) in the near wake of a rolling wheel at (*a*) $Re_D = 400$, (*b*) $Re_D = 500$, (*c*) $Re_D = 1000$. Eighteen contour levels are shown, with a colour scale from white to black, $0 \leqslant k/u_\infty^2 \leqslant 0.063$, $-0.024 \leqslant -\tau_{xy}/\rho_\infty u_\infty^2 \leqslant 0.024$.

of $Re_D \sim 10^5$ in experiments and real applications), the computed drag and lift coefficients (both of order unity here) are substantially larger than those measured in experiments. For instance, Fackrell & Harvey (1975) report $c_L = 0.44$, $c_D = 0.58$ for a real tyre in ground contact, with aspect ratio similar to that considered here. Nevertheless, we believe that this study can be instructive also for practical purposes, since many of the qualitative properties observed in high-Re_D experiments begin to appear at the higher Re considered here. Indeed, the structure of the flow field of the $Re_D = 1000$ simulation shows hints of turbulent behaviour in the wheel wake, which is reflected in the power spectra of the force coefficients, and it is not very different from the fields visualized in the experiments of Saddington *et al.* (2007) and Issakhanian *et al.* (2010). Specifically, a concentrated spanwise vortex is observed in the time-average fields right past the apex of the wheel, which is the result of the collapse of the top shear layer, and a spanwise vortex is observed near the aft contact point, which was also observed by Issakhanian *et al.* (2010). Particular significance is assumed by the wake structure in cross-stream planes, because of an existing controversy about the sign and direction of the quasi-streamwise vortices that are shed past the wheel. In this respect we find confirmation of recent experimental results (Issakhanian *et al.* 2010), which indicate two pairs of counter-rotating vortices. However, probably because of the limited Reynolds number that we are able to simulate, we also observe an additional vortex pair near the edge of the wheel. To conclude, we believe that DNS applied to the study of a rolling wheel, besides giving insight into the rich

physics of a computationally complex problem, could potentially lend some insight into practical problems. This DNS strongly supports the dynamical importance of complex vortex dynamics phenomena in the flow field, and suggests the importance of using unsteady flow simulations for its correct prediction, for which steady-type modelling approaches such as RANS are not suitable. Further efforts will be directed to establishing the validity of our Reynolds number extrapolation, and possibly to including simplified subgrid-scale LES turbulence models to access Reynolds numbers of direct practical relevance.

Acknowledgement

We acknowledge the CINECA award under the ISCRA initiative, for the availability of high-performance computing resources and support.

REFERENCES

ACARLAR, M. S. & SMITH, C. R. 1986 A study of hairpin vortices in a laminar boundary layer. Part 1. Hairpin vortices generated by a hemisphere protuberance. *J. Fluid Mech.* **175**, 1–41.

AXERIO, J., IACCARINO, G., ISSAKHANIAN, E., LO, K., ELKINS, C. & EATON, J. 2009 Computational and experimental investigation of the flow structure and vortex dynamics in the wake of a Formula 1 tire. *SAE Paper* 09B-0082.

BADR, H. M., COUTANCEAU, M., DENNIS, S. C. R. & MENARD, C. 1990 Unsteady flow past a rotating cylinder at Reynolds numbers 10^3 and 10^4. *J. Fluid Mech.* **220**, 459–484.

COGOTTI, A. 1983 Aerodynamic characteristics of car wheels. *Intl J Vehicle Design* **SP3**, 173–196.

DÉLERY, J. M. 2001 Robert Legendre and Henry Werlé: toward the elucidation of three-dimensional separation. *Annu. Rev. Fluid Mech.* **33**, 129–154.

FACKRELL, J. E. & HARVEY, J. K. 1973 The flow field and pressure distribution of an isolated road wheel. In *Advances in Road Vehicle Aerodynamics* (ed. H. S. Stevens), pp. 155–165. BHRA Fluid Engineering.

FACKRELL, J. E. & HARVEY, J. K. 1975 The aerodynamics of an isolated road wheel. In *Second AIAA Symposium on Aerodynamics of Sports and Competition Automobiles* (ed. B. Pershing), pp. 119–125. Western Periodicals Co.

FADLUN, E. A., VERZICCO, R., ORLANDI, P. & MOHD-YUSOF, J. 2000 Combined immersed-boundary finite-difference methods for three-dimensional complex flow simulations. *J. Comput. Phys.* **161**, 35–60.

FORNBERG, B. 1988 Steady viscous flow past a sphere at high Reynolds numbers. *J. Fluid Mech.* **190**, 471–489.

ISSAKHANIAN, E., ELKINS, C. J., LO, K. P. & EATON, J. K. 2010 An experimental study of the flow around a Formula 1 racing car tire. *Trans. ASME: J. Fluids Engng* **132**, 071103.

JEON, D. & GHARIB, M. 2004 On the relationship between the vortex formation process and cylinder wake vortex patterns. *J. Fluid Mech.* **519**, 161–181.

JOHNSON, T. A. & PATEL, V. C. 1999 Flow past a sphere up to a Reynolds number of 300. *J. Fluid Mech.* **378**, 19–70.

KANG, S., CHOI, H. & LEE, S. 1999 Laminar flow past a rotating circular cylinder. *Phys. Fluids* **11**, 3312–3321.

KATZ, J. 2006 Aerodynamics of race cars. *Annu. Rev. Fluid Mech.* **38**, 27–63.

MCMANUS, J. & ZHANG, X. 2006 A computational study of the flow around an isolated wheel in contact with the ground. *Trans. ASME: J. Fluids Engng* **128**, 521–530.

MITTAL, R. 1999*a* Planar symmetry in the unsteady wake of a sphere. *AIAA J.* **37**, 388–390.

MITTAL, R. 1999*b* Vortex dynamics in the sphere wake. *AIAA Paper* 99-3806.

MITTAL, S. & KUMAR, B. 2003 Flow past a rotating cylinder. *J. Fluid Mech.* **476**, 303–334.

MORELLI, A. 1969 Azioni aerodinamiche sulla ruota d'automobile. *ATA Review* **22**, 281–288.

ORLANDI, P. 1990 Vortex dipole rebound from a wall. *Phys. Fluids* A **2**, 1429–1436.

O'ROURKE, J. 1998 *Computational Geometry in C*. Cambridge University Press.

DE PALMA, P., DE TULLIO, M. D., PASCAZIO, G. & NAPOLITANO, M. 2006 An immersed boundary method for compressible viscous flow. *Comput. Fluids* **35**, 693–702.

PIROZZOLI, S. 2011 Numerical methods for high-speed flows. *Annu. Rev. Fluid Mech.* **43**, 163–194.

PIROZZOLI, S. & BERNARDINI, M. 2011 Turbulence in supersonic boundary layers at moderate Reynolds number. *J. Fluid Mech.* **688**, 120–168.

POINSOT, T. S. & LELE, S. K. 1992 Boundary conditions for direct simulations of compressible viscous flows. *J. Comput. Phys.* **101**, 104–129.

RAO, A., PASSAGGIA, P.-Y., BOLNOT, H., THOMPSON, M. C., LEWEKE, T. & HOURIGAN, K. 2012 Transition to chaos in the wake of a rolling sphere. *J. Fluid Mech.* **695**, 135–148.

SADDINGTON, A. J., KNOWLES, R. D. & KNOWLES, K. 2007 Laser Doppler anemometry measurements in the near-wake of an isolated Formula One wheel. *Exp. Fluids* **42**, 671–681.

STEWART, B. E., THOMPSON, M. C., LEWEKE, T. & HOURIGAN, K. 2010*a* Numerical and experimental studies of the rolling sphere wake. *J. Fluid Mech.* **643**, 137–162.

STEWART, B. E., THOMPSON, M. C., LEWEKE, T. & HOURIGAN, K. 2010*b* The wake behind a cylinder rolling on a wall at varying rotation rates. *J. Fluid Mech.* **648**, 225–256.

TAIRA, K. & COLONIUS, T. 2007 The immersed boundary method: a projection approach. *J. Comput. Phys.* **225**, 2118–2137.

TOBAK, M. & PEAKE, D. J. 1982 Topology of three-dimensional separated flows. *Annu. Rev. Fluid Mech.* **14**, 61–85.

TOMBOULIDES, A. G. & ORSZAG, S. A. 2000 Numerical investigation of transitional and weak turbulent flow past a sphere. *J. Fluid Mech.* **416**, 45–73.

WILLIAMSON, C. H. K. 1996 Vortex dynamics in the cylinder wake. *Annu. Rev. Fluid Mech.* **28**, 477–539.

WU, J.-S. & FAETH, G. M. 1993 Sphere wakes in still surroundings at intermediate Reynolds number. *AIAA J.* **31**, 1448–1455.

ZHOU, J., ADRIAN, R. J., BALACHANDAR, S. & KENDALL, T. M. 1999 Mechanisms for generating coherent packets of hairpin vortices in channel flow. *J. Fluid Mech.* **387**, 353–396.